Chapter 2
Analysis Techniques for *WMAP* Polarisation Data

In this chapter we describe the processing of the *WMAP* data and other full sky maps for the polarisation analysis. We start by describing the *WMAP* dataset. In Sect. 2.3 we describe the smoothed versions of the polarised maps and how we treated the noise after the smoothing. Next, in Sect. 2.5, we explain the polarisation bias correction scheme we used to obtain polarisation intensity maps. Section 2.5.5 shows the bias-corrected polarisation maps used later in this work. We then describe in Sect. 2.4 a filtering procedure that is used to remove the large scale emission from the maps in order to highlight the filamentary structure seen in the polarisation maps. Finally, in Sect. 2.6 we apply the de-biasing scheme for setting limits on the polarisation fraction of AME using *WMAP* data.

2.1 *WMAP* 9-Year Data

The description of the 9-year data can be found in Bennett et al. (2013). Here we summarise the main characteristics of the data. The 9-year data release encompasses observations from 00:00:00 UT 2001 August 10 to 00:00:00 UT 2010 August 10. The efficiency of the mission during this time is ∼98.4 %, where most of the data excluded belongs to intervals with low thermal stability.

The *WMAP* data processing scheme can be summarised as follows. The Time Ordered Data (TOD) are calibrated for each radiometer in order to convert the raw differential data into temperature units. This calibration is based on the CMB monopole temperature measured by *COBE* (Mather et al. 1999) and the dipole component, which is the Doppler-induced pattern product of the motion of the spacecraft in the CMB rest frame. A gain term (units of counts mK^{-1}) and baseline (units of counts) are used in this gain model. The 9-year analysis includes an additive ageing term for the radiometer in the form $m\,\Delta t + c$, where Δt is the elapsed mission time. The calibration scheme models the dipole variations with very small residuals. The estimate of the absolute calibration uncertainty takes a conservative value of 0.2 % (1σ) (Bennett et al. 2013). The efficiency factors of the two *WMAP* optical systems

M. Vidal Navarro, *Diffuse Radio Foregrounds*, Springer Theses,
DOI 10.1007/978-3-319-26263-5_2

differ slightly from one another. This accounts for time-independent *transmission imbalance factors* in the map making. There is good agreement between the 9-year values and the previous 7-year values within the uncertainties.

The mapping process of the calibrated TOD can be explained as follows. The TOD **d** for one particular radiometer can be described as

$$\mathbf{d} = \mathbf{M}\mathbf{t} + \mathbf{n}, \tag{2.1}$$

where **M** is the observing matrix, which contains information about the scan pattern and the beam shape. **M** converts the sky signal **t** into the TOD **d**. **n** is a vector representing the radiometer noise. The map is produced by inverting this equation and solving for **t**. The quality of the final map would depend on how well characterised are the constituents of the observation matrix.

The pointing of *WMAP* is computed using observations of Jupiter and Saturn, which are coupled to the orientation of the spacecraft using on-board star trackers. The estimated uncertainty on the pointing is $10''$.

The beam is characterised by azimuthally averaging beam maps obtained using observations of Jupiter. The 9-year data release includes a correction for the non-axisymmetric component of the beam for the Stokes I maps. It has been shown that the effect of asymmetric beams can affect the estimation of polarisation spectral indices (Wehus et al. 2013), so we will keep track of this effect later on. In Table 2.1 we list some characteristics of the *WMAP* instruments. The beam solid angle is listed for each channel as well as the FWHM of a Gaussian parametrisation of its shape. Also listed are the central frequency band and the bandwidth of each band. The central frequencies listed are for a point source with a temperature spectral index $\beta = -2.01$.

Table 2.1 *WMAP* characteristics

	K-Band	Ka-Band	Q-Band	V-Band	W-Band
Frequency (GHz)	22.69	32.94	40.62	60.52	92.99
Bandwidth (GHz)	5.5	7.0	8.3	14.0	20.5
Beam size[a] ($\times 10^{-5}$sr)	24.69	14.42	8.964	4.200	2.093
Beam width[b] (deg)	0.88	0.66	0.51	0.35	0.22
System temperature, T_{sys} (K)	29	39	59	92	145
Sensitivity (mK $s^{1/2}$)	0.8	0.8	1.0	1.2	1.6
$\sigma_0(I)$ (mK)[c]	1.429	1.466	2.188	3.131	6.544
$\sigma_0(Q, U)$ (mK)[c]	1.435	1.472	2.197	3.141	6.560

[a]Solid angle in azimuthally symmetrised beam profile
[b]FWHM of a Gaussian approximation to the beam profile
[c]Noise per observation in each pixel of the maps

2.1.1 WMAP *9-Year Maps*

The *WMAP* data are available as full sky maps at the five frequency bands. The Stokes I, Q and U maps are the final compact representation of the 9-year data. These maps are used to characterise the foreground emission, create a map of the CMB anisotropy and to perform the cosmological analysis. They are provided in the HEALPix[1] pixelisation scheme (Górski et al. 2005) with $N_{\rm side} = 512$, which corresponds to a pixel size of $\sim 7'$ (the sphere has $12 \times N_{\rm side}^2$ pixels). The data are in units of thermodynamic temperature which relates to antenna (brightness) temperature in the following way,

$$T_A = \frac{x^2 e^x}{(e^x - 1)^2} T_{thermo} \tag{2.2}$$

where $x = (h\nu)/(kT_0)$ and $T_0 = 2.726\,\mathrm{K}$ is the temperature of the CMB (Fixsen 2009).

Figure 2.1 shows a Mollweide projection of the full sky Stokes I maps at the angular resolution of each band listed in Table 2.1. The emission at K-band is dominated by diffuse Galactic foreground emission, mainly distributed along the Galactic plane. With increasing frequency (e.g. V and W bands), the level of foregrounds decreases, allowing the CMB to be clearly visible at high Galactic latitudes.

Figures 2.2 and 2.3 show the Stokes Q and U maps for each frequency. They are smoothed to a common resolution of 1°. In both Q and U, the strongest emission is observed at K-band. Figure 2.4 shows the polarisation amplitude, $P = \sqrt{Q^2 + U^2}$ for each frequency band. These maps are affected by polarisation bias and they have not been corrected for this effect. We will describe this bias in detail in Sect. 2.5.

Maps are supplied that describe the noise properties of the pixelated data, in terms of a number of observations ($\mathrm{N_{obs}}$) parameter. The total intensity noise maps for each frequency can be obtained using the following relation,

$$\sigma_I^2 = \frac{\sigma_0^2(I_p)}{N_{\rm obs}(I_p)} \tag{2.3}$$

with $\sigma_0(I_p)$ the noise per observation value in each pixel, listed in Table 2.1.

The noise in the polarisation maps is characterised by the covariance matrix, which includes the correlation term between Q and U. This correlation occurs mainly due to non-uniform azimuthal coverage for each pixel and fluctuations in the noise during the observations. The correlation is position-dependent and is characterised by the $N_{\rm obs}(QU)$ map. The covariance matrix for each pixel has the form,

$$\mathbf{C} = \begin{pmatrix} \sigma_Q^2 & \sigma_{QU} \\ \sigma_{QU} & \sigma_U^2 \end{pmatrix} = \sigma_0^2(QU) \begin{pmatrix} 1/N_{\rm obs}(QQ) & 1/N_{\rm obs}(QU) \\ 1/N_{\rm obs}(QU) & 1/N_{\rm obs}(UU) \end{pmatrix} \tag{2.4}$$

The $\sigma_0^2(QU)$ values for each band are also listed in Table 2.1.

[1] http://healpix.sourceforge.net/.

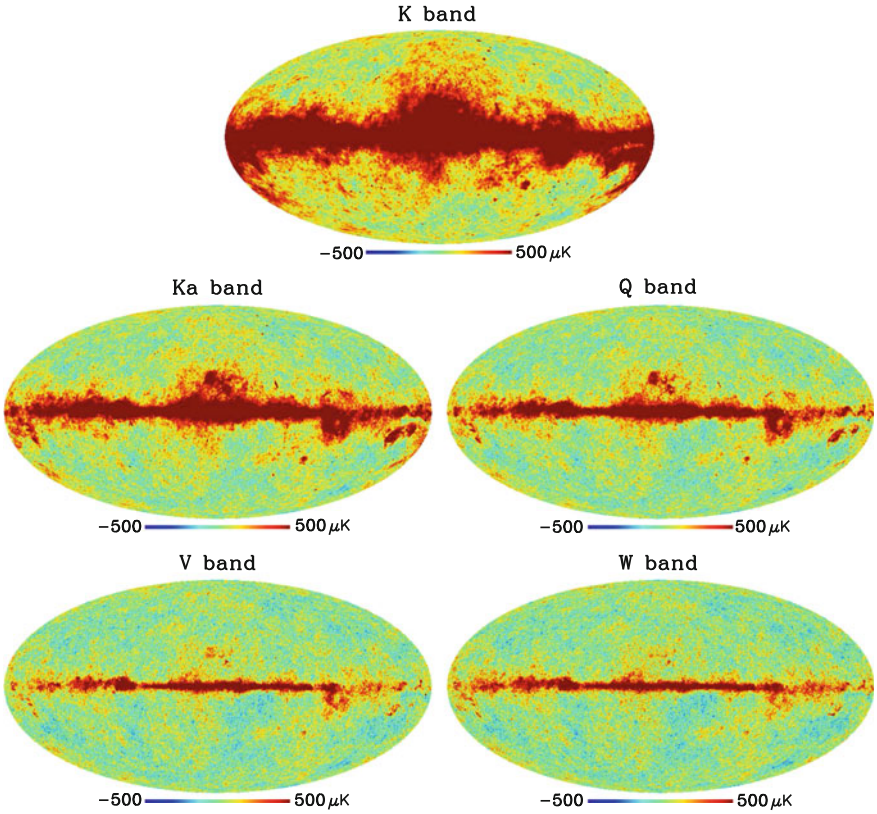

Fig. 2.1 *WMAP* 9-year Stokes I maps. The maps are displayed in a Galactic coordinate system using a Mollweide projection. The Galactic plane runs horizontally along the centre of each map. The Galactic longitude increases towards the left. The linear scale is the same in all maps, ranging from -500 to $500\,\mu$K in thermodynamics units. These maps have the original angular resolution at each band, as listed in Table 2.1

In Fig. 2.5, we show the noise maps for K-band, where the σ_I, σ_Q, σ_U and σ^2_{QU} maps are shown. The structure in these maps is revealing the spacecraft observing pattern during the 9 year of data collection. The large circular features visible in them are centred at the ecliptic poles, which are the regions of the sky with the largest integration time. Similar maps exist for all the frequency bands but due to their similarity, here we only show the ones corresponding to K-band.

We note that the noise maps shown here do not include any systematic effects. Fluctuations in the gain of the receivers, thermal instabilities and noise temperature fluctuations in the TOD will produce correlated noise in the final maps. This type of noise, referred as "$1/f$ noise" is not normally distributed. In general, the instrumental noise of *WMAP* data (or any similar instrument) can be described as the sum of white (Gaussian) and correlated noise. The power spectral density of the noise has the form,

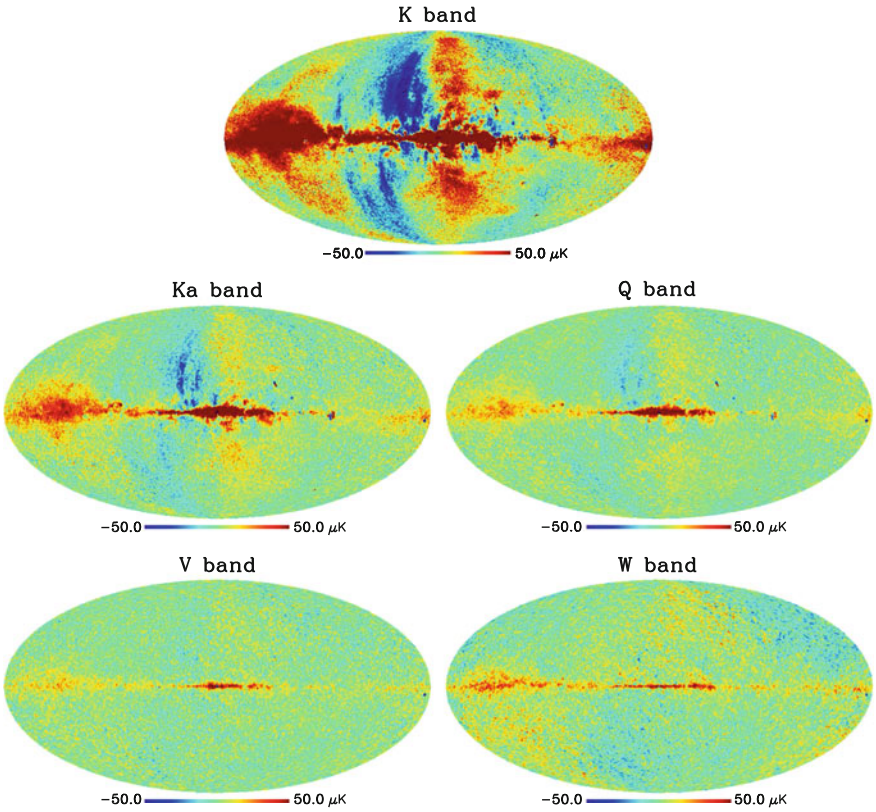

Fig. 2.2 *WMAP* 9-year Stokes Q maps. The linear scale is the same in all maps, ranging from -50 to $50\,\mu$K in thermodynamics units. The maps have been smoothed to a common resolution of 1°

$$P_{\text{noise}} = \left[1 + \left(\frac{f_k}{f}\right)^{\alpha}\right] \frac{\sigma}{f_s}, \tag{2.5}$$

where f_k is called the "knee" frequency, f_s is the sampling frequency of the data and σ is the standard deviation of the white noise during the sample integration time ($t = 1/f_s$). For *WMAP* data, the $1/f$ component of the noise is modelled and subtracted from the data, leaving small residuals. The covariance along the scan directions is limited to be less than 0.1 % for the K, Ka, Q and V bands (Hinshaw et al. 2003). The W–band presents the worst $1/f$ noise, which is at least a factor 3 larger than the rest of the bands (Jarosik et al. 2003). This small contribution from "1/f" noise allows us to use only the white noise maps shown here to quantify the uncertainties of the data.

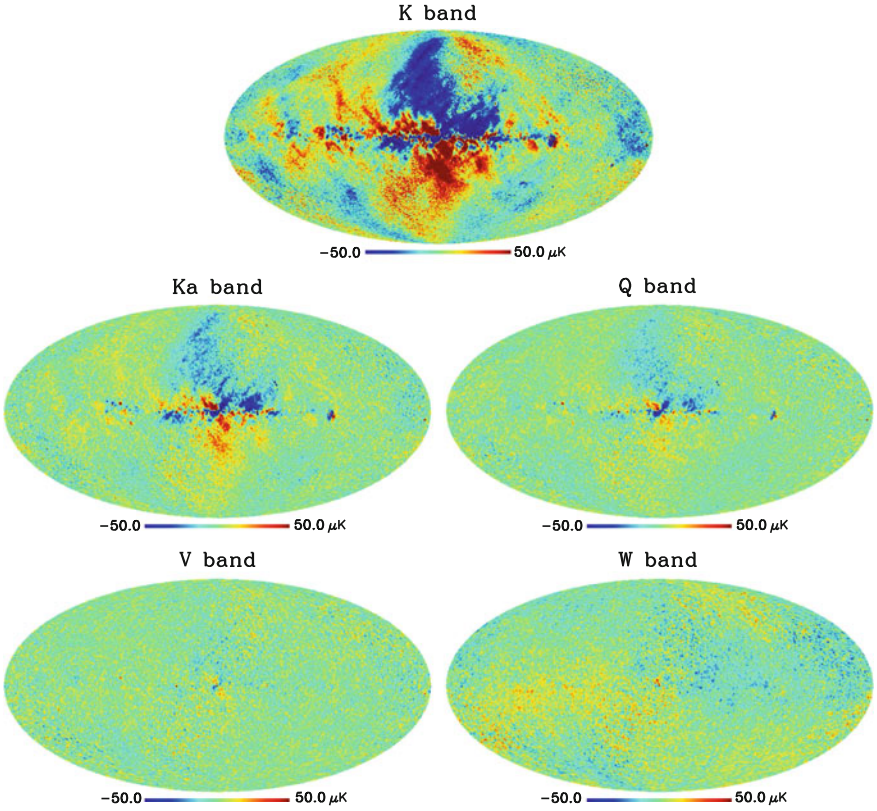

Fig. 2.3 *WMAP* 9-year Stokes *U* maps. The linear scale is the same in all maps, ranging from −50 to 50 μK in thermodynamics units. The maps have been smoothed to a common resolution of 1°

2.2 *WMAP* Sky Simulation

In order to test the results that we will present in this chapter and also in Chap. 3, we used a simulation of the synchrotron emission in *WMAP* data using the *Planck* Sky Model.

The Planck Sky Model (PSM) (Delabrouille et al. 2013), is a software package that implements modelling of the emission mechanisms at GHz frequencies with the aim of creating a realistic representation of the sky emission in both total intensity and polarisation. The PSM can model the CMB emission, SZ effect, extragalactic sources and the Galactic emission. There are five diffuse Galactic components: synchrotron, free-free, AME, thermal dust and CO molecular lines. In this case, we have simulated only the synchrotron emission as it is dominant in *WMAP* polarisation data. The synchrotron simulation is based on the model by Miville-Deschênes et al. (2008), which uses *WMAP* seven-year data and the 408 GHz map by Haslam et al. (1982) to fix its parameters. The simulations are created using a resolution parameter $N_{\text{side}} = 512$.

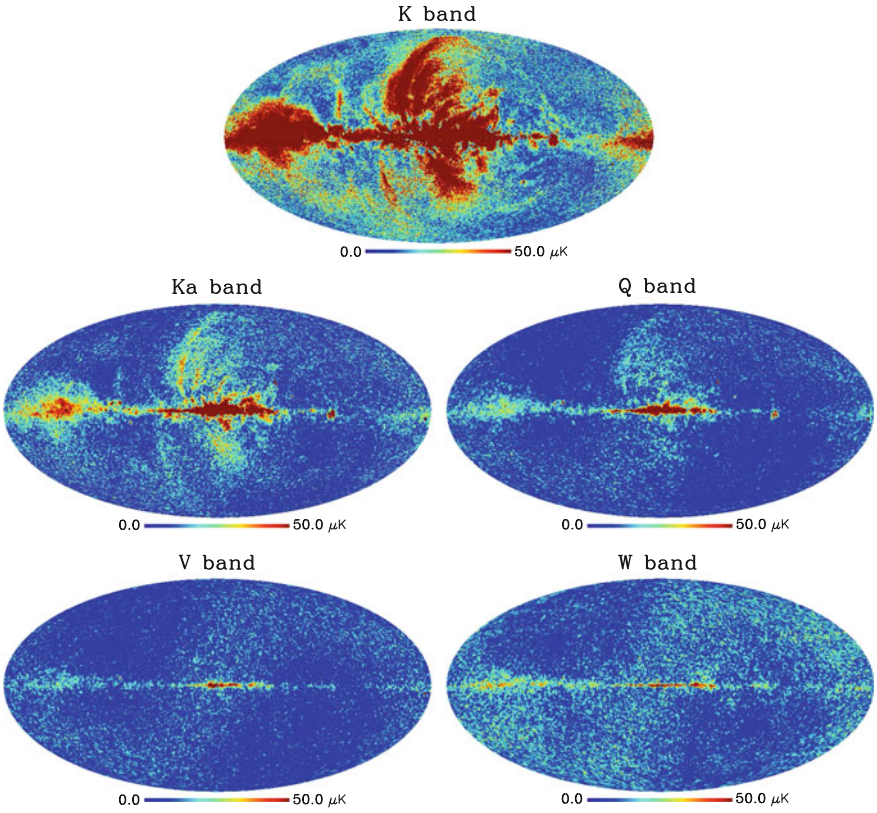

Fig. 2.4 *WMAP* 9-year polarisation amplitude $P = \sqrt{Q^2 + U^2}$ maps. The linear scale is the same in all maps, ranging from 50 to 50 μK in thermodynamics units. The maps have been smoothed to a common resolution of 1°

Figure 2.6 shows the templates for Stokes I, Q, U and the polarisation amplitude at K-band as observed by *WMAP* . There is no noise added to these simulations. The Q, U and P maps shown here are similar to the *WMAP* polarisation data shown in Figs. 2.2, 2.3 and 2.4.

2.3 Smoothing

To increase the signal-to-noise-ratio (SNR) of the maps, and to minimise any systematic effect due to beam-asymmetries in polarisation, we smoothed the maps to common resolutions of 1° and 3° full-width-half-maximum (FWHM). This was done using HEALPix by first deconvolving in harmonic space the azimuthally symmetrized effective beam and then convolving with a Gaussian beam. The *WMAP* team

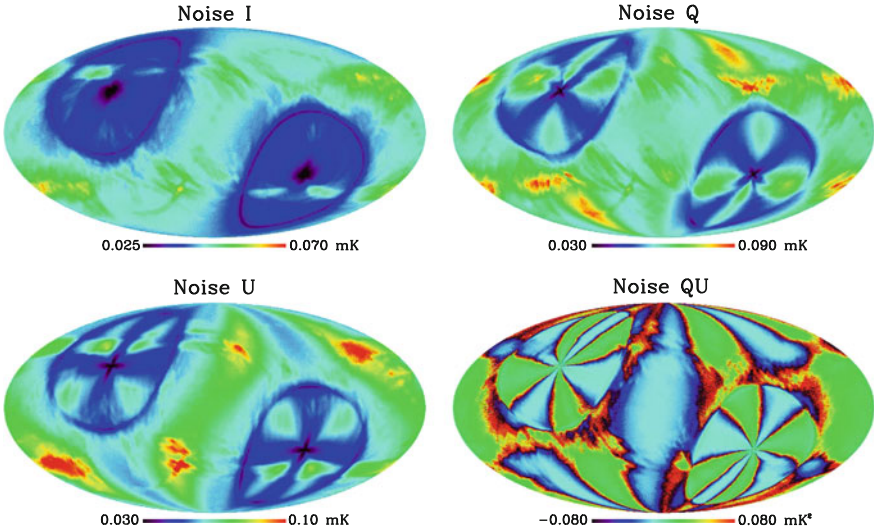

Fig. 2.5 *WMAP* 9-year K-band noise per pixel maps. On *top*, are the σ_I and σ_Q maps, and at the *bottom*, the σ_U and σ^2_{QU} maps. The structure in these maps is related to the *WMAP* scanning pattern

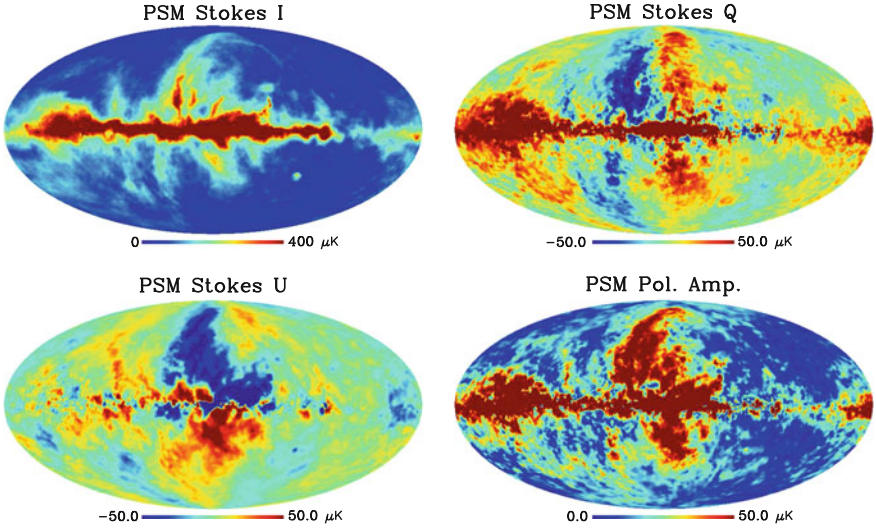

Fig. 2.6 Planck Sky Model templates for synchrotron emission as observed by *WMAP* at K-band. On *top* are Stokes I and Q, at the *bottom* are Stokes U and the polarisation amplitude map. These simulations do not include noise

provides the symmetrized beam transfer functions derived from the observations of Jupiter, B_ℓ^S, which describe the response of the antenna as a function of multipole. For the precision that the cosmological analysis requires, the *WMAP* beams have been very well characterised. We take advantage of the available transfer functions, instead of the commonly used Gaussian approximation for the beam. The convolution of the maps with a Gaussian beam corresponds to a multiplication in harmonic space of the $a_{\ell,m}$ representation of the map with an "effective" transfer function, defined by,

$$B_\ell^{eff} = e^{-\frac{1}{2}\ell(\ell+1)\sigma^2}/B_\ell^S, \tag{2.6}$$

where σ is the width of the smoothing Gaussian beam in radians.[2]

In Fig. 2.7 we show the symmetrised transfer functions for each *WMAP* band. Note the difference between the symmetrised beam transfer function in black, and the Gaussian parametrisation of the beam based on a Gaussian approximation in red, with a width equal to the values listed in Table 2.1. The largest deviations from a Gaussian beam occur for the higher frequency bands. The blue line is the effective transfer function used for the smoothing to obtain a map with an angular resolution of 1° FWHM.

For the spectral index analysis that we will present in the next chapter, we smoothed the polarisation maps to a common angular resolution of 3°. The choice of this smoothing scale is a compromise between having a good SNR across a large area of the sky and having enough spatial resolution to characterise the observed structures. Wehus et al. (2013) showed that the beam asymmetries in *WMAP* K- and Ka-bands give rise to unstable spectral index measurements in polarisation on 1° scales. Here, with an effective resolution of 3°, the asymmetries have minimal impact.

The propagation of the uncertainty in the maps after smoothing with a Gaussian kernel $G(\sigma^2)$ defined by its standard deviation σ, can be calculated analytically to create a new "smoothed" variance map N' if the errors are independent and normally distributed,

$$N'^2 = \frac{\Omega}{4\pi\sigma^2} N^2 \otimes G(\sigma^2/2), \tag{2.7}$$

with Ω the solid angle of each pixel. Note that the smoothing width, $\sigma/\sqrt{2}$, is different from the smoothing kernel of the map (σ).

Unfortunately, this is not valid for *WMAP* data. The noise is correlated at large angular scales. Moreover, in polarisation the covariance matrix is not diagonal as there are correlations between the uncertainties in Q and U. In order to asses the noise level after the smoothing of the maps, we used Monte Carlo simulations, which are described in the next Section.

[2]Note that σ relates with the FWHM by the relation $\sigma = \mathrm{FWHM}/\sqrt{8\ln 2}$.

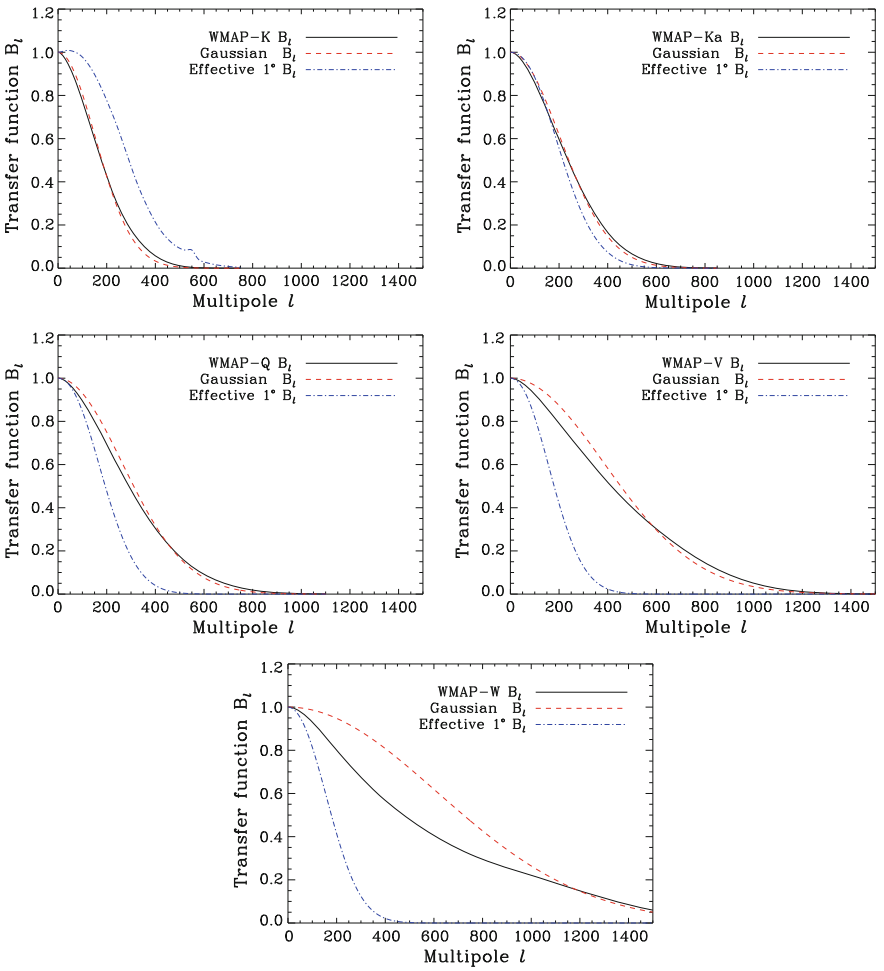

Fig. 2.7 The plots show the beam transfer functions as function of multipole for the five *WMAP* channels. In *black* is the symmetrised beam function as characterised by the *WMAP* team. In *red* is the Gaussian transfer function with a width equivalent to the ones tabulated in Table 2.1. Note the discrepancies between the "true" beam shape in *black* and the equivalent Gaussian in *red*. In *blue* is the effective beam transfer that we used to smooth the maps to a common 1° angular resolution FWHM

2.3.1 WMAP *Noise Simulations*

We ran Monte Carlo simulations to calculate the uncertainties after the smoothing and pixel downgrading. We generated 500 normally distributed noise realisation for Stokes I, Q and U for each frequency band using the covariance matrix from the

WMAP data. The covariance matrix is constructed for each pixel in the following way:

$$\mathbf{C} = \sigma_0^2(QU) \begin{pmatrix} N_{QQ} & N_{QU} \\ N_{QU} & N_{UU} \end{pmatrix}^{-1} \tag{2.8}$$

where $\sigma_0^2(QU)$ is the nominal polarisation noise per observation listed in Table 2.1 for each frequency band and N_{QQ}, N_{QU} and N_{UU} are the $N_{\rm obs}$ maps supplied with the data. We used the IDL routine MRANDOMN to draw each realisation of the noise. This routine uses a Cholesky decomposition of the covariance matrix to efficiently generate random deviates from a multivariate normal distribution. The output of the simulation are 500 noise maps for Stokes I, Q and U.

We calculated the statistics of this assembly and we used the dispersion on each pixel (for the I, Q, and U maps) as the statistical error on the 3° smoothed maps. We also calculated the covariance term between Q and U for the ensemble (σ^2_{QU}). By this route, we have smoothed maps for Stokes I, Q and U with their respective uncertainties and (Q, U) correlations for each pixel. For all the noise values estimated, we need to add in quadrature the 0.2 % *WMAP* absolute calibration error (Bennett et al. 2013).

2.3.2 Optimal N_{side}

After smoothing, the 3° resolution maps at $N_{\rm side}$ = 512 are over-sampled, i.e. there are too many pixels (∼778) per beam area. Ideally, the pixel size should be similar to the beam size. The re-pixelisation onto a coarser grid (less and bigger pixels) of a scalar quantity, such as the total intensity brightness temperature is straightforward, the values of the smaller pixels are averaged into a single value that is given to the new, larger pixel.

When working with polarisation, more care is required. The polarisation of any given pixel has an amplitude and a direction, and both quantities should be adequately transformed onto the coarser grid. The standard re-pixelisation procedure (averaging of smaller pixels to form a new larger one) can induce systematic errors in the new polarisation maps, which are more prominent close to the coordinates poles. Parallel transport has to be used in order to produce adequate re-pixelisation of polarisation maps. The HEALPix package includes a routine (`ud_grade`) to upgrade/degrade a full sky map in the HEALPix scheme. Unfortunately, this routine does not include parallel transport and therefore, is not reliable close to the poles.

An alternative to downgrade the maps in this case is to generate new maps, in a new grid, from the pseudo-scalar E and B-modes spectra. To do this, we first used the HEALPix routine `anafast` to create the power spectra of the polarisation maps. We save the $a_{\ell,m}$ coefficients and they are fed to the routine `synfast`, which creates a new map using the power spectra in a grid defined by the user. By this way, the new map is created with correct polarisation information. A problem with this method

is that the fast Fourier transform (FFT) involved in the computation of the power spectra produces artefacts in the final map, which are more important around sharp features of the map (e.g. strong point sources, the Galactic plane).

In practise, the effect of using or not parallel transport is very small and it is only important close to the poles. In Fig. 2.8 we compare two polarisation maps P_1 and P_2 produced with the two methods described above. Both maps are downgraded versions of a 3° smoothed map from an original $N_{side} = 512$ to $N_{side} = 32$. P_1 is produced with the `ud_grade` routine without parallel transport; P_2 is produced with `anafast` + `synfast`, regridding the $a_{\ell,m}$ onto a coarser grid. The figure shows the difference between P_1 and P_2 divided by the polarisation noise σ_P, calculated simply as $\sigma_P = \sqrt{Q^2\sigma_Q^2 + U^2\sigma_U^2 + 2QU\sigma_{QU}^2}/P$ (this is not an accurate quantification of the polarisation noise as the quantity $P = \sqrt{Q^2 + U^2}$ has a positive bias which will be discussed in detail in Sect. 2.5, nevertheless, is a good approximation for the display purposes here).

In Fig. 2.8, the most obvious differences occur at the regions with larger signal, like the Galactic plane. They are due to FFT artefacts in the map produced using `anafast` + `synfast`. The level of these artefacts will be a function of the ℓ_{max} values adopted in `anafast`. We have used $\ell_{max} = 3 \cdot N_{side} - 1$. This way, the spherical harmonics form a linearly independent system. The difference between the two studied maps is small, the scale in the figure shows the $\pm 0.5\,\%$ range in terms of the polarisation noise. From the lower panel of the figure, we see the red blobs at the Galactic poles. This difference between the two maps at the poles is due to the parallel transport difference between the two polarisation maps. As this effect is smaller than the larger artefacts seen on the Galactic plane, we can safely ignore them in our analysis.

For the rest of this work, we will use the maps degraded using `ud_grade`, ignoring the parallel transport issues, as they are relatively small compared with the artefacts produced by the second method.

Test on spectral index estimation with different pixel sizes

We tested the effect of different pixel sizes on the estimation of the polarised spectral index (in Sect. 3.3 we discuss the polarised spectral indices in detail). For this, we used the PSM simulation at K-band described in Sect. 2.2. We scale this polarisation template to 33 GHz using an input spectral index $\beta = -3.0$. Then, we added a noise realisation using the *WMAP* covariance matrix. The idea of this test is to check if the measured spectral index and its uncertainty from these simulated maps varies with different pixel sizes.

The spectral index is measured over the entire map using the T-T plots approach (see Sect. 3.3 for a detailed description on this). The full-sky mean value and its uncertainty as a function of the pixel size is plotted in Fig. 2.9. In this figure, the measured spectral indices and their uncertainty are not visibly affected by the pixel size used. Here, the measured central value for β is not exactly the input value of $\beta = -3.0$, this is because used only one noise realisation. Nevertheless, what it is important is the consistency of the measured values with different pixel size.

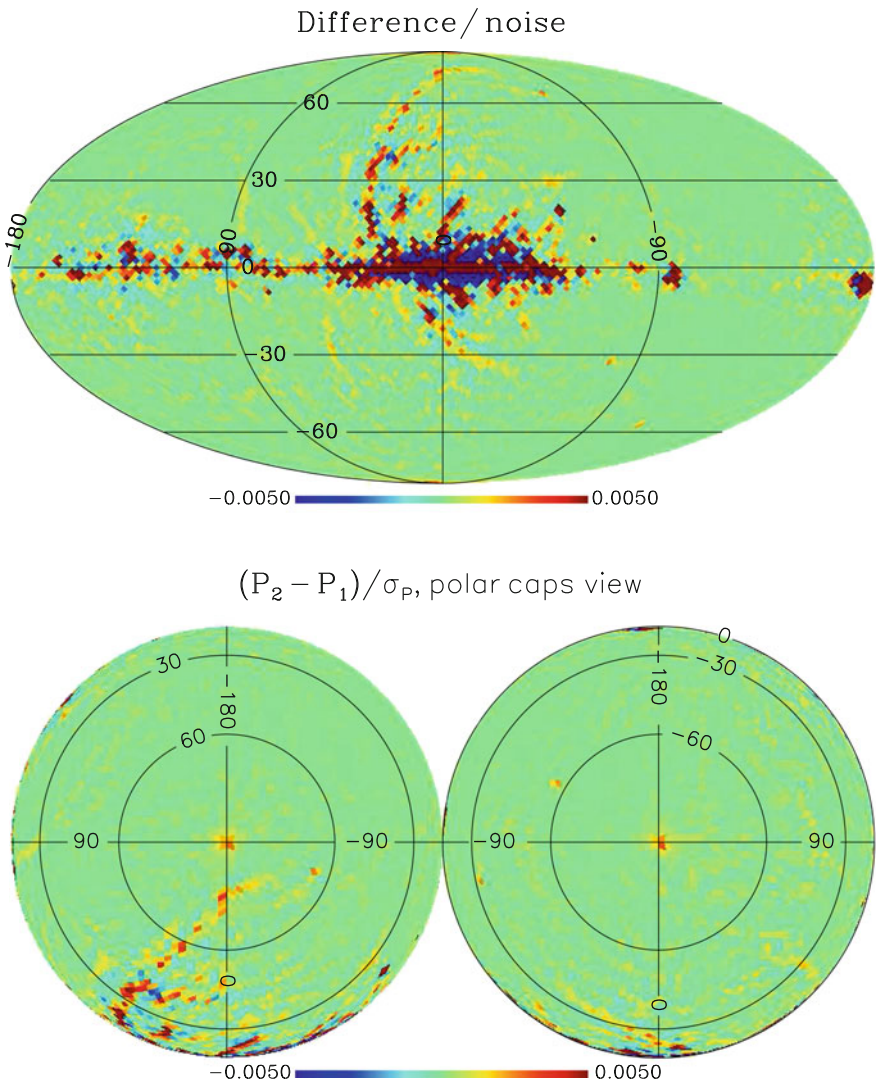

Fig. 2.8 Comparison between two *WMAP* K-band polarisation maps degraded from $N_{side} = 512$ to $N_{side} = 32$ using two methods: *i.* the routine `ud_grade`, which does not take into account parallel transport and *ii.* a re-mapping from the power spectra using the `anafast` and `synfast` routines. The difference is then divided by the uncertainty in the polarisation amplitude, σ_P. On *top* is a Mollweide projection showing the entire sky map. At the *bottom* is an orthographic projection centred at the north and south Galactic poles. Note the differences around the poles, seen as a two *red circular* regions

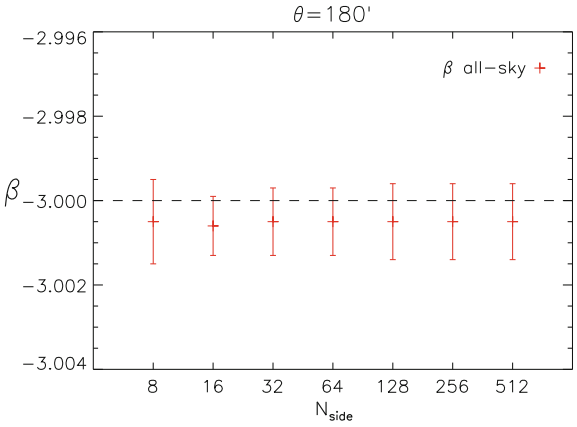

Fig. 2.9 Variation of the uncertainty in the polarisation spectral index as a function of the resolution parameter N_{side} for 3° resolution maps. β is calculated using 2 simulated maps at K– and Ka-band with a fiducial spectral index $\beta = -3.0$. The quoted error bar shows the error on the mean of the measured spectral index on the entire sky. There is no variation on the measured spectral index with different pixel size

This analysis allows us to choose the optimal pixel size that keeps the information of the spatial structures and allow us faster computation and analysis of the maps. This is $N_{side} = 32$ for the maps smoothed to 3°. For the maps that are smoothed to 1°, we use $N_{side} = 64$, which corresponds to pixel size ≈54'.9.

2.4 Unsharp Mask

A convenient image-processing technique can be used in order to highlight certain features from a sky map. Here we describe the *unsharp masking* technique, which works as a spatial high-pass filter, washing-out features that are larger than a defined angular scale. We will use this technique in Chap. 3 to identify the filaments visible in the *WMAP* polarisation maps.

We start with an initial map of brightness temperature T. This map T is convolved with a Gaussian beam $G(\sigma)$ to produce $\widetilde{T}_0$:

$$T \otimes G = \widetilde{T}_0. \tag{2.9}$$

We then define:

$$\delta T_0 = T - \widetilde{T}_0, \tag{2.10}$$

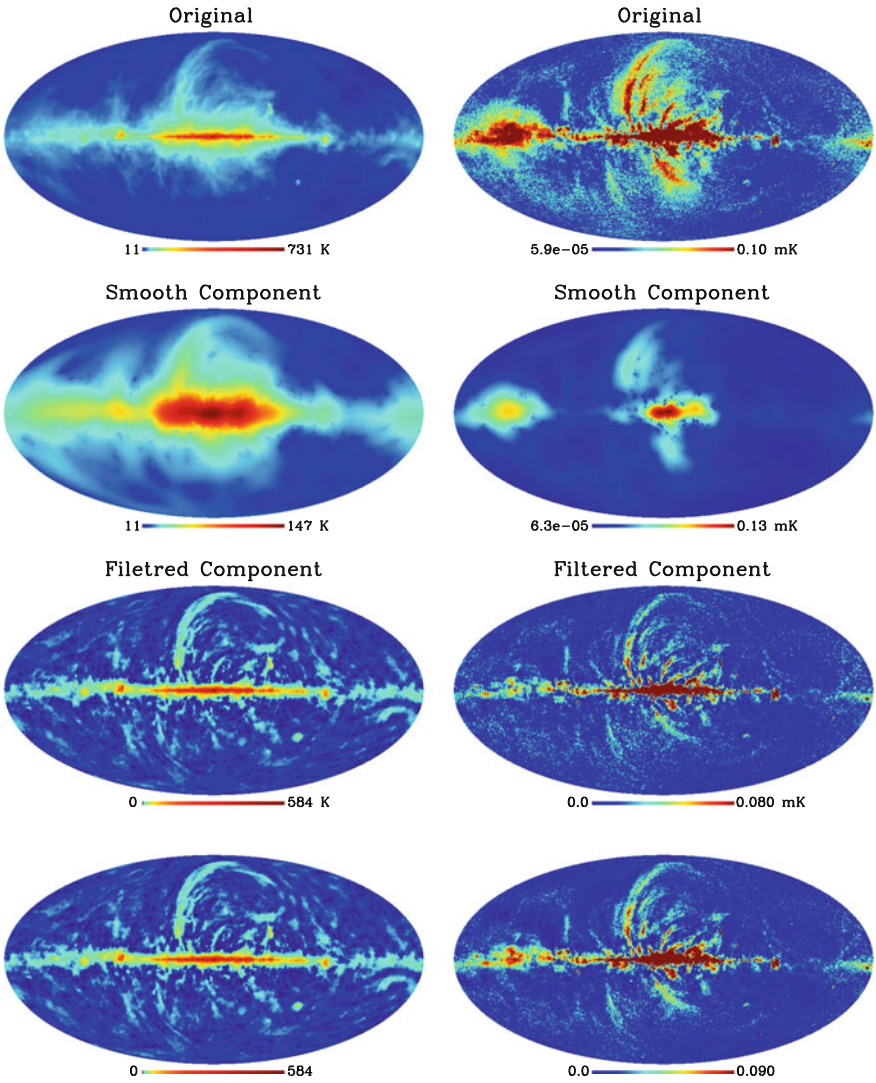

Fig. 2.10 Images illustrating the unsharp mask technique on two full-sky maps, the 408 MHz Haslam et al. (1982) map on the *left* column and the *WMAP* K-band polarisation map on the *right*. On *top* are shown the original maps, both of them smoothed to a common resolution of 1°. In the *middle*, is the smooth component, calculated using the iterative process described in the text. At the *bottom* are the filtered maps, highlighting the filamentary structure present in both maps. The convolution kernel has a size of 5° FWHM

which maps the small-scale (compared to the smoothing kernel) component of the original map. We also define

$$T_1 = \begin{cases} T - \delta T_0, & \text{if} \quad \delta T_0 > 0 \\ T, & \text{if} \quad \delta T_0 \leq 0. \end{cases} \tag{2.11}$$

T_1 is equal to the original map T except in the small-scale structures ($\delta T_0 > 0$), where it takes the value of $\widetilde{T}_0$.

T_1 is then convolved with the same Gaussian kernel $G(\sigma)$ to produce $\widetilde{T}_1$, ΔT_1 and T_2. This process is repeated i-times, until T_i converges to a unique background or until,

$$|T_i - T_{i-1}| < \sigma_T, \tag{2.12}$$

where σ_T is the RMS noise per pixel of the map, based in the number of observations in *WMAP* data. At this stage, T_i will be a template of the smooth large scale component of the original map. The unsharp-masked map is then defined by $T_{unsharp} = T - T_i$.

In Fig. 2.10 we show two examples of the process applied to the 408 MHz map from Haslam et al. (1982) map and to the *WMAP* K-band polarisation amplitude map. Both maps are initially smoothed to a common resolution of 1°. Then, the unsharp masking processes is executed, using a 5° Gaussian as the smoothing kernel. In the figure, the original maps (T), the large scale component (T_i) and the final filtered maps ($T_{unsharp}$) are shown. We will discuss and use these filtered maps in the next chapter.

2.5 Polarisation Bias

It has long been noticed that observations of linear polarisation are subject to bias (Serkowski 1958). Given the positive nature of $P = \sqrt{Q^2 + U^2}$, even if the true Stokes parameters are zero, P will yield a non-zero estimate in the presence of noise. The effect is particularly important in the low SNR regime. In this section we review different estimators used in the literature, propose an alternative one, more suitable for *WMAP* data and finally we test the efficiency of the different methods using Monte Carlo simulations.

Ways to correct for the bias have been studied in detail (Quinn 2012; Simmons and Stewart 1985; Vaillancourt 2006; Wardle and Kronberg 1974) for the special case where the uncertainties for (Q, U) are equal and normally distributed around their true value (Q_0, U_0). We will first review this case and then study the more general case with unequal uncertainties in (Q, U).

2.5.1 Symmetric Uncertainties

Let us take (Q_0, U_0) as the true Stokes parameters from a source and (Q, U) the measured ones. We can write the joint probability distribution function (p.d.f.) for (Q, U) as the product of the individual normal distributions

$$f(Q,U) = \frac{1}{2\pi\sigma^2}\exp\left(-\frac{(Q-Q_0)^2+(U-U_0)^2}{2\sigma^2}\right), \tag{2.13}$$

where $\sigma_Q = \sigma_U = \sigma$ is the uncertainty in (Q, U).

Transforming into polar coordinates using the definitions from Eq. 1.5,

$$\begin{aligned} f(P,\chi) =& \frac{P}{\pi\sigma^2}\exp\left(-\frac{P^2+P_0^2-2(P\cos 2\chi P_0\cos 2\chi_0 + P\sin 2\chi P_0 \sin 2\chi_0)}{2\sigma^2}\right) \\ =& \frac{P}{\pi\sigma^2}\exp\left(-\frac{P^2+P_0^2}{2\sigma^2}\right)\exp\left(-\frac{PP_0\cos[2(\chi-\chi_0)]}{\sigma^2}\right). \end{aligned} \tag{2.14}$$

The marginal probability distribution for P is obtained by integrating $f(P, \chi)$ over χ. This angular integral can be written as a function of the modified Bessel function of first type $I_0(z)$ (Vinokur 1965), yielding the Rice distribution for polarisation

$$R(P|P_0) = \frac{P}{\sigma^2} I_0\left(\frac{PP_0}{\sigma^2}\right) e^{-\frac{P^2+P_0^2}{2\sigma^2}}. \tag{2.15}$$

It is important to note that the integral of $R(P|P_0)$ represents the probability of measuring P inside an interval for a *known* true polarisation P_0. Figure 2.11 shows $R(P|P_0)$ for different SNR. The bias, defined as $\langle P\rangle - P_0$, arises as this probability distribution is not symmetric and becomes clear in Fig. 2.11 at low SNR levels. Even

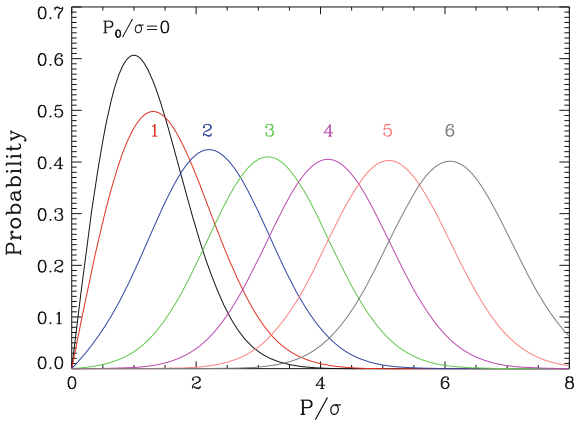

Fig. 2.11 Rice distribution (Eq. 2.15) plotted for different values of the true SNR, P_0/σ. The asymmetry and bias are clear in the low SNR level. At high SNR, the distribution converges to a Gaussian with standard deviation σ centred at P_0

when the true SNR is zero (black curve in the Figure), the measured value is close to 1. At large SNR, the mean of the distribution approaches a Gaussian with mean close to P_0 and standard deviation close to σ.

If Eq. 2.14 is integrated with respect to P, it yields the probability distribution of the polarisation angle χ. This distribution for χ is given by Naghizadeh-Khouei and Clarke (1993) and Quinn (2012):

$$G(\chi|\chi_0, P_0, \sigma) = \frac{1}{\sqrt{\pi}}\left(\frac{1}{\sqrt{\pi}} + \eta_0 e^{\eta_0^2}[1 + \mathrm{erf}(\eta_0)]\right) e^{-\frac{P_0^2}{2\sigma^2}}, \tag{2.16}$$

with $\eta_0 = \frac{P_0}{\sqrt{2}\sigma}\cos[2(\chi - \chi_0)]$ and erf is the Gaussian error function.

Simmons and Stewart (1985) describe four estimators of P_0 that are better surrogates for P.

- The median estimator $\hat{p}_M$ defined as the value for which the observed value P equals the median of the distribution $R(P|P_0)$.
- The mean estimator $\hat{p}_S$ defined as the value for which the observed value P equals the mean of the distribution $R(P|P_0)$.
- The Wardle and Kroberg's estimator $\hat{p}_{WK}$ which is obtained when the observed polarisation is a maximum of $R(P|P_0)$, that is

$$\left.\frac{\partial R}{\partial P}(P, P_0)\right|_{P_0=\hat{p}_{WK}} = 0. \tag{2.17}$$

  Therefore, $\hat{p}_{WK}$ satisfies

$$I_0\left(\frac{\hat{p}_{WK}P}{\sigma^2}\right)\left(1 - \frac{\hat{p}_{WK}^2}{\sigma^2}\right) + \frac{\hat{p}_{WK}P}{\sigma^2} I_1\left(\frac{\hat{p}_{WK}P}{\sigma^2}\right) = 0. \tag{2.18}$$

  Wardle and Kronberg (1974) propose an analytic approximation to solve this equation valid for $P/\sigma > 1$. The estimator

$$\hat{p}_{WK} \approx \sqrt{P^2 - \sigma^2} \tag{2.19}$$

  performs accurately for SNR $\gtrsim 2$.
- The maximum likelihood estimator $\hat{p}_{ML}$, is the value of P_0 that maximises $R(P|P_0)$ for a given observed polarisation P, that is

$$\left.\frac{\partial R}{\partial P_0}(P, P_0)\right|_{P_0=P_{WK}} = 0. \tag{2.20}$$

  Note that this is not equivalent to Eq. 2.17 as the differentiation in this case is with respect to P_0. $\hat{p}_{ML}$ can be found by evaluating numerically the following expression for a given P,

$$PI_0\left(\frac{\hat{p}_{ML}P}{\sigma^2}\right) - \hat{p}_{ML}I_1\left(\frac{\hat{p}_{ML}P}{\sigma^2}\right) = 0. \tag{2.21}$$

Simmons and Stewart (1985) conclude that the maximum likelihood estimator is superior for low SNR ($P_0/\sigma \lesssim 0.7$) and the Wardle and Kroberg's estimator $\hat{p}_{WK}$ performs better for higher SNR. The median and mean estimator are the best only in a very narrow SNR region. When the SNR is large, ($P_0/\sigma > 4$), all estimators converge. In this case, it is more convenient the simpler representation of $\hat{p}_{WK}$ (Eq. 2.19).

2.5.2 Asymmetric Uncertainties

As we saw, the previous case in which the uncertainties in (Q, U) are equal is well understood and solved for a fair range of SNR. The asymmetric case ($\sigma_Q \neq \sigma_U$) is interesting as many polarisation data sets have this characteristic. In particular, the correlations between the (Q, U) uncertainties in *WMAP* data are mainly due to non-uniform azimuthal coverage for each pixel in the sky and fluctuations in the noise during the observations. The error probability distribution in this case is an elliptical 2D Gaussian in (Q, U), in which the semi-axis correspond to the uncertainties in (Q, U), σ_Q and σ_U. In Fig. 2.12 are shown the histograms of the eccentricity[3] of the error ellipses for all the pixels in the five *WMAP* bands.

When the uncertainties in (Q, U) are not equal, the polarisation bias depends also in the polarisation angle χ as well as on p. A generalisation of the Wardle and Kronberg estimator can be written for this case. It has the form:

$$\hat{p}_{wk} = \sqrt{P'^2 - (\sigma_Q^2 \sin^2 2\chi' + \sigma_U^2 \cos^2 2\chi' - 2\sigma_{QU} \cos 2\chi' \sin 2\chi')}. \tag{2.22}$$

This estimator reduces to Eq. 2.19 when the errors are isotropic. Here, the observed polarisation angle, χ' is used as a surrogate for the true polarisation angle χ. At the high SNR regime (e.g. the bright regions in *WMAP* K-band), the approximation $\chi' \approx \chi$ is excellent. In the low SNR case, the answer is not straightforward and the only way to test this is to measure the residual bias of the estimator. We will discuss simulations that we use to measure the performance of this estimator in Sect. 2.5.4.

The estimator in Eq. 2.22 can be used to de-bias the polarisation maps at K-band, where there is a reasonable SNR along large areas of the sky. For the rest of the bands, where the SNR is much lower we can derive a new estimator. For this, we use the fact that we can obtain a good estimation of the *true* polarisation angle χ from *WMAP* K-band. Moreover, at *WMAP* frequencies, Faraday rotation is negligible over most of the sky (see Sect. 3.4) so we can assume that the polarisation angle χ

[3]The eccentricity, e, is defined as $e = \sqrt{1 - \left(\frac{\sigma_{\rm min}}{\sigma_{\rm maj}}\right)^2}$, where $\sigma_{\rm min}/\sigma_{\rm maj}$ correspond to the minor/major axial ratio of the ellipse.

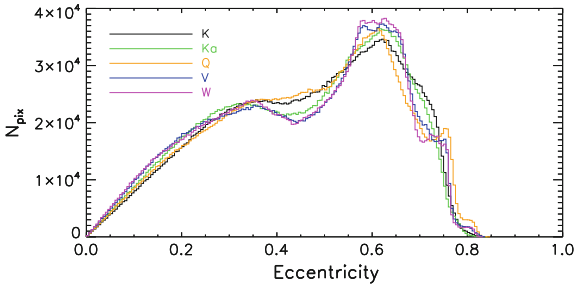

Fig. 2.12 Histograms of the eccentricity of the polarisation probability distribution of *WMAP* data. The histograms are made using the full sky maps at the original angular resolution (see Table 2.1), with N_{side} = 512

observed at K-band, will be the same at the higher frequency bands. The additional information about the polarisation angle in the higher frequency bands will help to reduce the total bias in the pixels with low SNR. In the next section we derive this new estimator, assuming that we know the true polarisation angle χ. In Sect. 2.5.4 we use simulations to test the effectiveness of this new estimator and to quantify any residual bias due to noise in χ.

2.5.3 *Known Angle Estimator*

We will build a new estimator assuming that the true polarisation angle χ is know, without any bias or noise. Later we will test the effect of these assumptions with simulations. This estimator can be used when a good independent measurement of the polarisation angle is available.

From Bayes theorem, the posterior p.d.f. for P, given the observed values (P', χ') is given by

$$f(P|\mathbf{P}', \chi') = \frac{f(\mathbf{P}', \chi'|P) f(P', \chi')}{\int f(\mathbf{P}', \chi'|P) f(P', \chi') dP' d\chi'} \tag{2.23}$$

where $f(\mathbf{P}', \chi'|P) \equiv L(P)$ is the likelihood function of P and $f(P', \chi')$ is the prior p.d.f. for P.

Knowing χ and assuming a uniform prior for P (all values for the amplitude of P are equally probable), we have

$$f(P|\mathbf{P}', \chi_0) \propto f(\mathbf{P}', \chi_0|P). \tag{2.24}$$

The maximum likelihood estimator in this case, $\hat{p}_{\chi_0}$, is defined as the value that maximizes $f(\mathbf{P}', \chi_0|P)$.

To find $\hat{p}_{\chi_0}$, we start by writing the joint p.d.f. for the observed values (Q, U) with asymmetric uncertainties

$$f(P|Q', U') = \frac{1}{2\pi\sigma_Q\sigma_U\sqrt{1-\rho^2}} e^{\left(-\frac{1}{2(1-\rho^2)}\left[\frac{(Q-Q')^2}{\sigma_Q^2}+\frac{(U-U')^2}{\sigma_U^2}-\frac{2\rho(Q-Q')(U-U')}{\sigma_Q\sigma_U}\right]\right)}, \quad (2.25)$$

where ρ is the correlation coefficient between (Q, U), defined as

$$\rho = \frac{E[(Q-Q')(U-U')]}{\sigma_Q\sigma_U} = \frac{\sigma_{QU}}{\sigma_Q\sigma_U}. \quad (2.26)$$

Using that $Q = P\cos 2\chi$ and $U = P\sin 2\chi$ in Eq. 2.25,

$$f(P|Q', U') = \frac{1}{2\pi\sigma_Q\sigma_U\sqrt{1-\rho^2}} e^{\left(-\frac{1}{2(1-\rho^2)}\left[\frac{(P\cos 2\chi-Q')^2}{\sigma_Q^2}+\frac{(P\sin 2\chi-U')^2}{\sigma_U^2}-\frac{2\rho(P\cos 2\chi-Q')(P\sin 2\chi-U')}{\sigma_Q\sigma_U}\right]\right)}. \quad (2.27)$$

$\hat{p}_{\chi_0}$ is defined by the condition,

$$\left.\frac{\partial f(P|Q', U')}{\partial P}\right|_{P=\hat{p}_{\chi_0}} = 0. \quad (2.28)$$

This finally leads to the expression for the de-biased polarisation amplitude,

$$\boxed{\hat{p}_{\chi_0} = \frac{\sigma_U^2 Q'\cos 2\chi - \sigma_{QU}(Q'\sin 2\chi + U'\cos 2\chi) + \sigma_Q^2 U'\sin 2\chi}{\sigma_U^2\cos^2 2\chi - 2\sigma_{QU}\sin 2\chi\cos 2\chi + \sigma_Q^2\sin^2 2\chi}}. \quad (2.29)$$

We note that if the "observed" position angle $\chi' = 0.5\arctan(U'/Q')$ differs by more than 45° from χ, $\hat{p}_{\chi_0}$ will have a negative value. We also note that this estimator is not valid when the observed polarisation angle is used as a surrogate for χ_0. In that case, $\hat{p}_{\chi_0} = p'$ and there is no correction whatsoever. This means that we cannot use this method, for instance, to correct *WMAP* K-band if we are using the angle information from K-band data as well. However, it can be used to correct Ka, Q, V and W bands using the additional polarisation angle information from K band.

We would also like to have confidence intervals for this estimator. For this, we use the following definitions

$$\begin{aligned} Q &= P\cos 2\chi, & U &= P\sin 2\chi \\ Q' &= \hat{p}_{\chi_0}\cos 2\chi_0, & U' &= \hat{p}_{\chi_0}\sin 2\chi_0, \end{aligned} \quad (2.30)$$

and with the assumption that we know the *true* value for $\chi = \chi_0$, we obtain

$$\begin{aligned} Q - Q' &= \cos 2\chi (P - \hat{p}_{\chi_0}) \\ U - U' &= \cos 2\chi (P - \hat{p}_{\chi_0}). \end{aligned} \tag{2.31}$$

Then, Eq. 2.25 can be written in the form

$$\begin{aligned} f(P|\bar{p}) &\propto e^{\left(-\frac{\sigma_U^2 \cos^2 2\chi (P-\hat{p}_{\chi 0})^2 + \sigma_Q^2 \sin^2 2\chi (P-\hat{p}_{\chi 0})^2 - 2\rho\sigma_Q\sigma_U \cos 2\chi \sin 2\chi (P-\hat{p}_{\chi 0})^2}{2(1-\rho^2)\sigma_Q^2\sigma_U^2}\right)} \\ f(P|\bar{p}) &\propto e^{-\frac{(P-\hat{p}_{\chi 0})^2}{2\sigma_{\hat{p}}^2}}, \end{aligned} \tag{2.32}$$

with

$$\boxed{\sigma^2_{\hat{p}_{\chi_0}} = \frac{\sigma_Q^2\sigma_U^2 - \sigma_{QU}^2}{\sigma_U^2 \cos^2 2\chi - 2\sigma_{QU} \sin 2\chi \cos 2\chi + \sigma_Q^2 \sin^2 2\chi}}. \tag{2.33}$$

This is the variance of the $\hat{p}_{\chi_0}$ estimator.

2.5.4 *Tests of the Estimators*

We compared the effectiveness of the de-biasing methods using Monte Carlo simulations for a range of SNR. First, we study the residual bias in a single pixel for a range of SNR in (Q, U). Then we tested the methods in simulations using the *WMAP* covariance matrices.

General case

Using Monte Carlo simulations, we measure the residual bias in a single pixel for three polarisation amplitude estimators:

- $\hat{p} = P' = \sqrt{q'^2 + u'^2}$; i.e. the naive estimator with no correction for the bias.
- $\hat{p}_{wk} = \sqrt{P'^2 - (\sigma_Q^2 \sin^2 2\chi' + \sigma_U^2 \cos^2 2\chi' - 2\sigma_{QU} \cos 2\chi' \sin 2\chi')}$; the generalised Wardle and Kronberg estimator for asymmetric uncertainties from Eq. 2.22.
- The known angle estimator $\hat{p}_{\chi_0}$, presented in Eq. 2.29.

We first create a grid of 100×100 different values of Q/σ_Q and U/σ_U, in the range $0 \leq Q/\sigma_Q < 10$, $0 \leq U/\sigma_U < 10$, using a uniform spacing. The value of σ_Q is fixed to $\sigma_Q = 1$ while σ_U is scaled using a fixed value for the ratio between the (Q, U) uncertainties (if there are no correlations, $\sigma_Q = \sigma_U = \sigma$). Then, 10^5 Gaussian noise realisations are added to the each point in the grid. The noise realisations have a standard deviation of $\sigma = \sigma_U = 1$. By this way, we have $100 \times 100 \times 10^5$ "observed" values for (Q', U') values.

We then calculated the "observed" polarisation amplitude, $P' = \sqrt{Q'^2 + U'^2}$ from the noisy simulations. We applied the estimators to each simulation and we measured

the fractional mean bias for each pixel in the grid, $(\langle\hat{p}\rangle - P_0)/P_0$. The first column of Fig. 2.13 shows the fractional bias of the naive estimator P' using four different values for the error ellipse eccentricity e. In all the simulations, $\sigma_{QU} = 0$. This does not affect the generality of the results because the covariance σ_{QU} can always be set to zero by a rotation of the (Q, U) axes. The second column in Fig. 2.13 shows contours of the fractional mean bias after using the generalised Wardle and Kronberg estimator. The biased regions in the SNR plane reduces considerably in comparison with the first column that has no correction.

The third column of Fig. 2.13 shows the residual bias using the $\hat{p}_{\chi_0}$ estimator. This estimator requires an independent value for the polarisation angle along with the observed values (Q', U') and their standard deviation. We generated additional 10^5 Gaussian realisations for the polarisation angle, centred at the true value, χ_0, for each SNR value. The standard deviation in the angle distribution is fixed to 1°.9,[4] which means that we are in an ideal case where we know with high accuracy the true polarisation angle. The residual bias of this estimator is very small, less than 5 % over most of the parameter space as can be seen in the four right-hand panels of Fig. 2.13.

In the previous ideal case, when the real polarisation angle is known accurately, the known-angle estimator performs much better than the generalised Wardle and Kronberg. This situation with very small uncertainty in the polarisation angle is not very common, so we also quantified the bias using simulations with a larger uncertainty in the polarisation angle. Figure 2.14 shows contours for the mean bias averaged over 10^5 Gaussian realisations, centred at the true polarisation angle χ_0 for three values of the uncertainty in the polarisation angle $\sigma_\chi = 2°.8,\ 5°.7$ and 9°.5 (these values corresponds to a SNR in polarisation of 10, 5 and 3 respectively for the case where $\sigma_Q = \sigma_U$).

Figure 2.14 shows that the known angle estimator over corrects the polarisation amplitude by a small amount (less than 5 %) if the uncertainty in the polarisation angle is lower than ∼6° (central column). If the uncertainty in the polarisation angle is larger, the negative bias can be as high as 10 %. We note that the last row of the figure shows that this over correction can be as bad as −30 %. However, the large eccentricity in this case ($e = 0.9$) does not occur at least in *WMAP* data (see Fig. 2.12).

We can see that the known angle estimator works particularly well in the case when the polarisation angle is well known. An uncertainty in the input polarisation angle up to ∼6° produces, in the worst scenario, a negative bias of 5 %. The exact values will depend on the polarisation angle of each particular pixel. In the next Section we test the debiasing methods using the *WMAP* noise properties.

WMAP **case**

In *WMAP* data, the five frequency maps present different SNR. This is due to a combination between the nature of the observed emission (synchrotron has

[4] 1°.9 corresponds to a SNR of 15 in the polarisation amplitude in the case where the uncertainties are symmetric (Naghizadeh-Khouei and Clarke 1993).

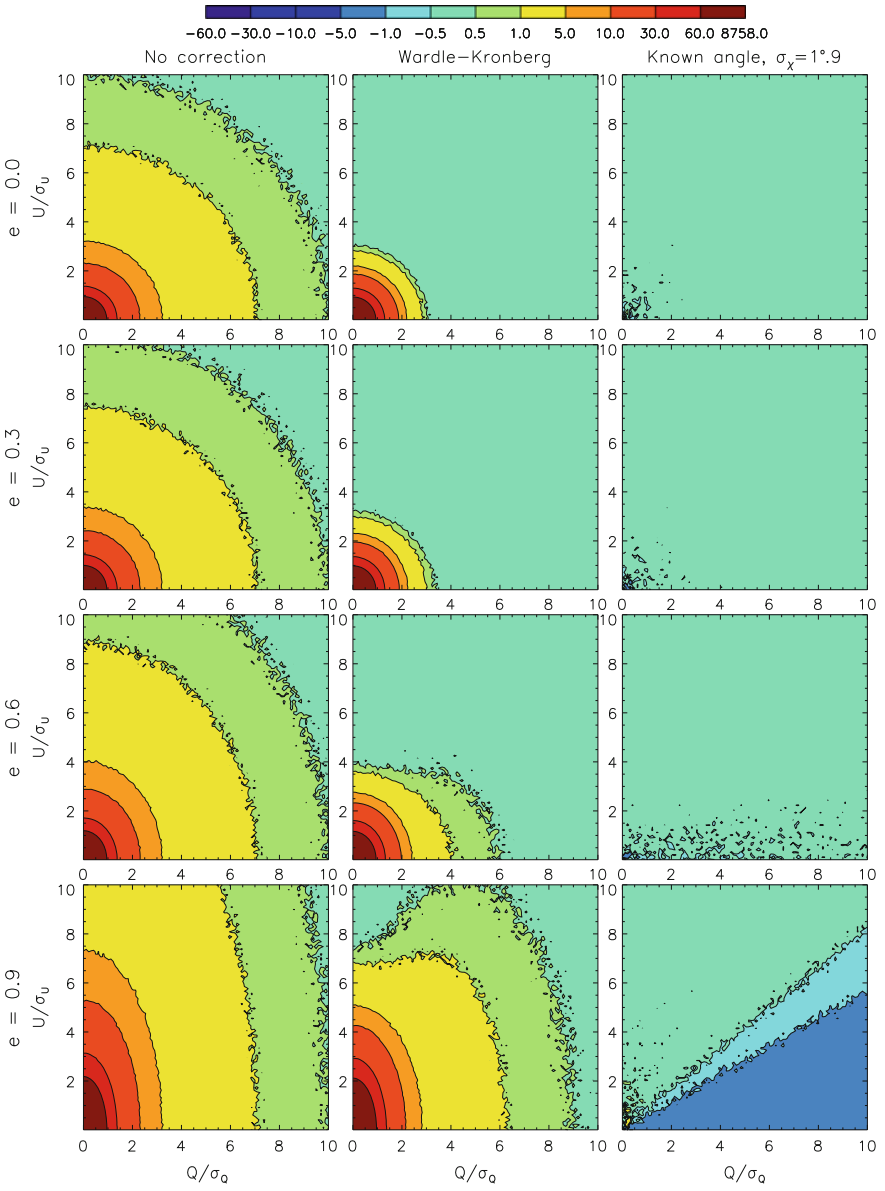

Fig. 2.13 Contours of the fractional mean residual bias of three estimators for the polarised intensity as a function of (Q, U). In each plot, $\sigma_Q = 1$ and $\sigma_{QU} = 0$ (note that there is no loss of generality as the covariance can always be eliminated by a rotation of the $Q - U$ axes). The colour scale represents the percentage bias of the estimated polarisation value for each pixel

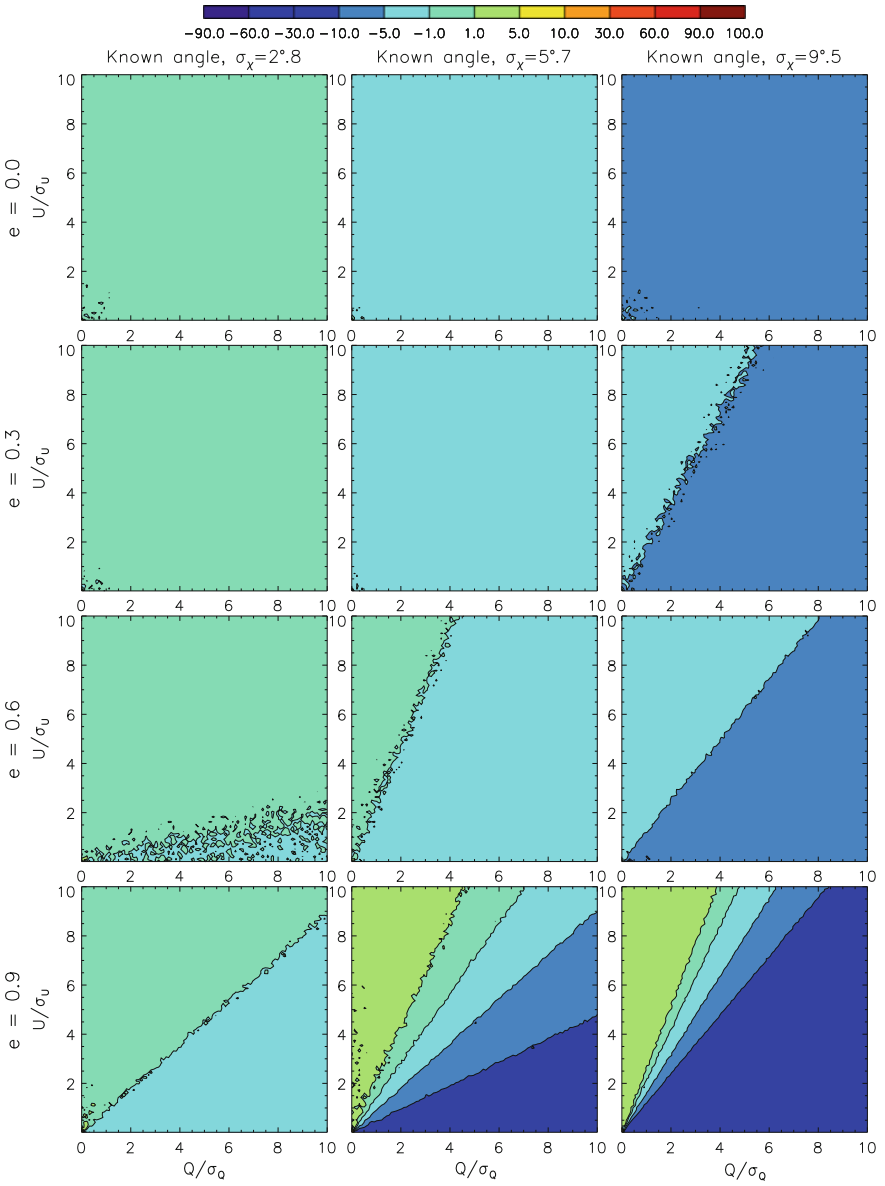

Fig. 2.14 Contours of the mean residual bias of the known angle estimator for three values of the uncertainty in the fiducial polarisation angle (*columns*) and four values for the eccentricity of the error ellipse (*rows*). The colour scale represents the percentage bias of the estimated polarisation value for each pixel

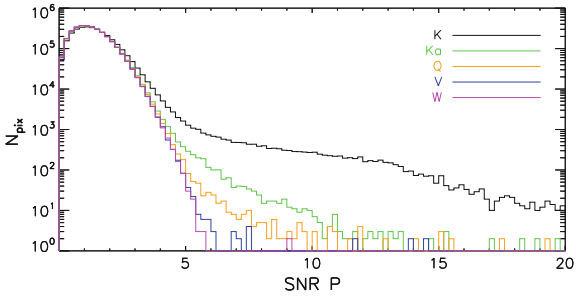

Fig. 2.15 Histograms of the SNR of the polarisation probability distribution of *WMAP* data. The histograms are made using the full sky maps at the original angular resolution of each map, with $N_{side} = 512$

a negative spectral index) and the variation in sensitivity along the bands (see Table 2.1). *WMAP* K-band has a higher SNR in polarisation, where large areas of diffuse emission present SNR > 3. Figure 2.15 show histograms of the SNR for the Stokes parameters (Q, U) of the five frequency bands. The polarisation SNR in K-band is larger than the SNR in the other bands for almost the entire sky. Also, the SNR in the Ka-, Q-, V- and W-bands is rarely larger than 3.

We used the *Planck* Sky Model simulation of the polarised sky at K-, Ka- and Q-bands at an angular resolution of 1°, from which we can obtain maps for the unbiased polarisation amplitude, P_0. We added random noise (generated using the *WMAP* covariance matrices, in a similar way as described in Sect. 2.3.1) to the simulated Stokes Q and U maps. With these noisy maps, we produce the "observed" polarisation amplitude, P, maps.

We corrected for the bias in these P maps using both the Wardle and Kronberg's method and the $\hat{p}_\chi$ estimator described earlier. The angle information required by the $\hat{p}_\chi$ estimator is measured from the K-band map. This implies that we cannot use the $\hat{p}_\chi$ estimator to correct the K-band map (it is exactly the same as doing no correction whatsoever and $\hat{p}_\chi = P$ as mentioned in Sect. 2.5.3). We then compared these debiased maps with the true polarisation amplitude map from the PSM simulations. In Table 2.2 we list the bias value, averaged over the entire sky for the three bands that we studied.

The absolute mean bias, $\langle \Delta p_0 \rangle = \langle P - P_0 \rangle$ (no correction applied) is larger as the frequency increases towards Q-band due to the decrease in SNR. For Ka- and Q-bands, the p_χ estimator performs much better than p_{WK}. We can see this better

Table 2.2 Full-sky averaged values for the polarisation bias, for three estimators

Estimator	K-band μK	Ka-band μK	Q-band μK
$\langle \Delta p_0 \rangle$	0.9 ± 0.1	2.5 ± 0.1	3.00 ± 0.1
$\langle \Delta p_{WK} \rangle$	0.4 ± 0.1	2.0 ± 0.1	2.7 ± 0.1
$\langle \Delta p_\chi \rangle$	0.9 ± 0.1	-0.2 ± 0.1	-0.1 ± 0.1

The first row list the "absolute bias", i.e. the difference between the noisy polarisation amplitude and the true value for P. The second row lists the residual bias, after using the Wardle and Kroberg's method. The third row list the averaged bias values for the $\hat{p}_{\chi_0}$ estimator. Note that in K-band, the $\hat{p}_{\chi_0}$ estimator is not correcting for the bias and that is why the estimated value is equal to the uncorrected value in the first row

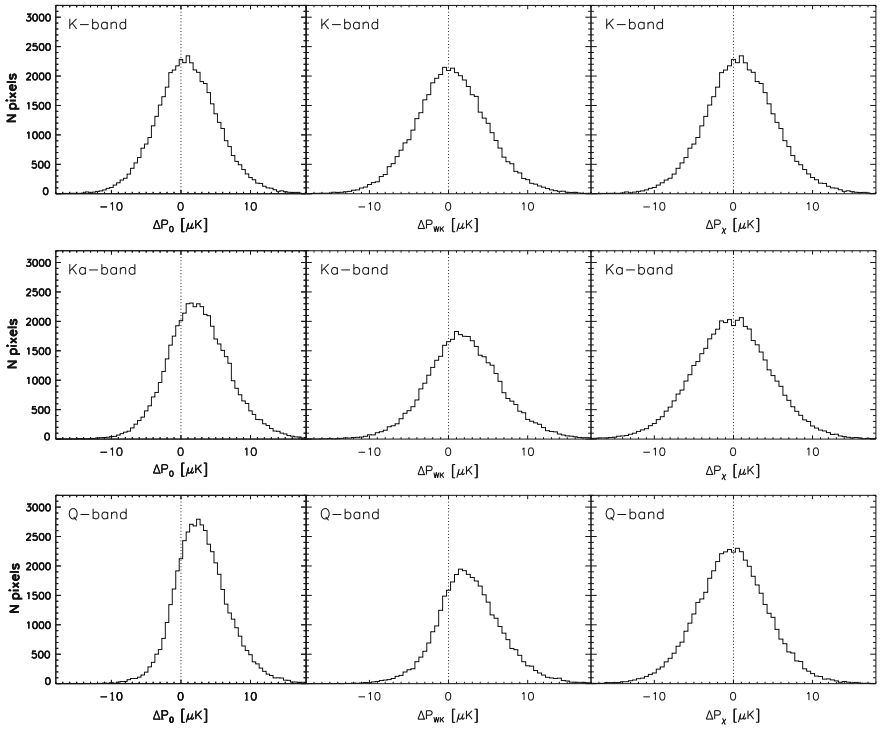

Fig. 2.16 Histograms showing the bias of the three estimators studied. A simulation of the polarised sky at K-, Ka- and Q-band using the Planck sky model is used. The noise present in *WMAP* data is added to each one of the simulated Q, U maps. The histograms show the distribution of the difference between the three estimators and the true polarisation amplitude P'. The column on the *left* shows the histograms of the absolute bias, i.e. the $\Delta P_0 = P_0 - P'$ (no bias correction). The central column shows ΔP using the Wardle and Kronberg estimator, $\Delta P_{WK} = p_{WK} - P'$. For the noisier bands (*Ka* and *Q*), the histograms are not centred at zero, implying that there is additional residual bias on the corrected map. On the *right* the histograms produced using the $\hat{p}_\chi$ estimator, $\Delta P_{WK} = p_\chi - P'$. Here the bias correction works much better and the distributions for the three bands are centred at zero. Table 2.2 lists the central values and uncertainties for all the histograms

by looking at the histograms in Fig. 2.16. In Ka- and Q-band, the bias is clear, the histograms of the uncorrected polarisation maps are not centred at zero (the three plots on the *left*). The Wardle and Kronberg estimator, p_{WK} in the central column, is less biased but in Ka and Q bands there is still a clear shift from the zero value. The p_χ estimator on the right column corrects for the bias much better at the three frequencies, as the three distributions are centred at zero.

In order to see where the residual bias is more important, we show maps of the fractional bias after the correction using the different estimators. Figure 2.17 shows the fractional bias at K-band for the naive estimator $P = \sqrt{Q^2 + U^2}$ and the Wardle and Kronberg estimator $\hat{p}_{WK}$ defined in Eq. 2.22 (the map with the residual bias from the $\hat{p}_{\chi_0}$ estimator is not shown as in this case is equal to the uncorrected estimator).

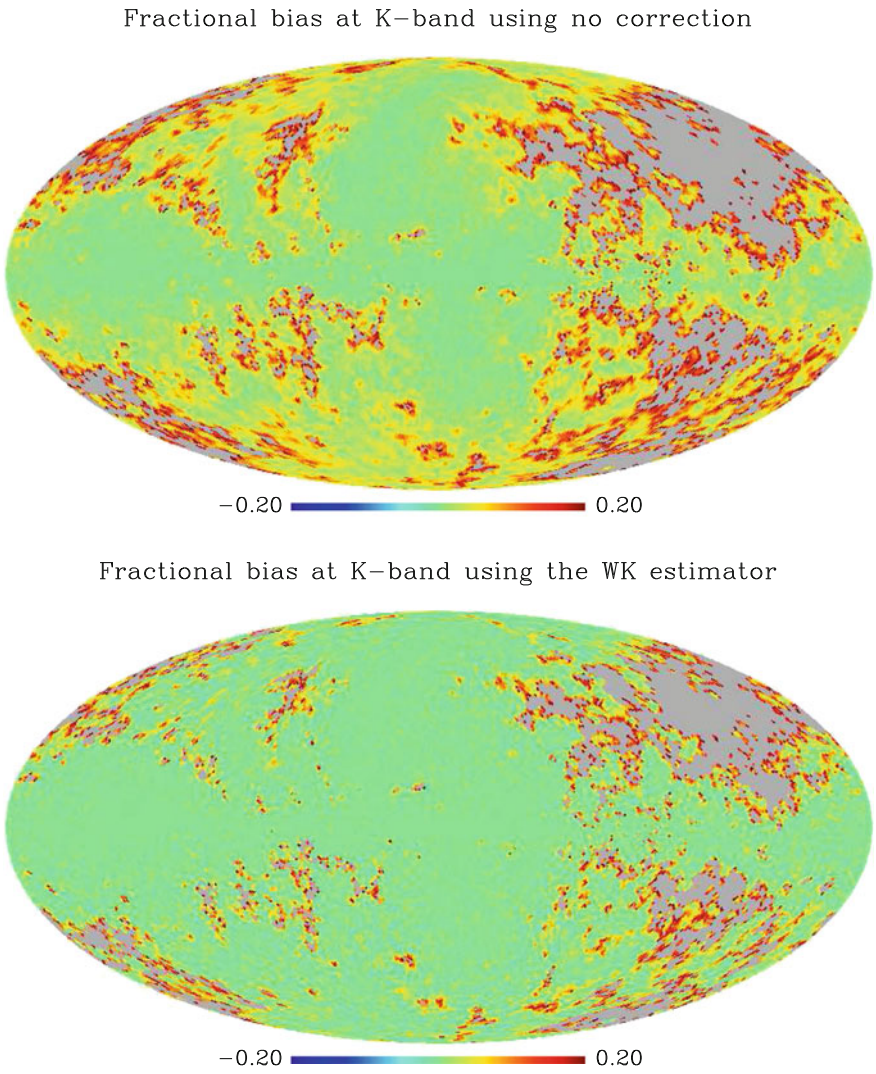

Fig. 2.17 Maps showing the fractional bias at K-band. On *top* is the polarisation bias for the naive estimator $P = \sqrt{Q^2 + U^2}$. At the *bottom* is the residual bias that remains after correcting with the $\hat{p}_{WK}$ estimator. All the pixels with a value larger than 20 % (0.2 in the map units) are shown in *grey*. They corresponds to the regions with lower SNR

In the Figure, the pixels where the residual bias is larger than 20 % are shown in grey. The $\hat{p}_{WK}$ estimator leaves a small residual bias over most of the sky (green areas in the Figure).

Figures 2.18 and 2.19 show similar maps for Ka and Q-bands. Here, the residual fractional bias map from the $\hat{p}_{\chi_0}$ estimator have been included. The pixels with an absolute value of the residual bias larger than 20 % have also been masked as grey.

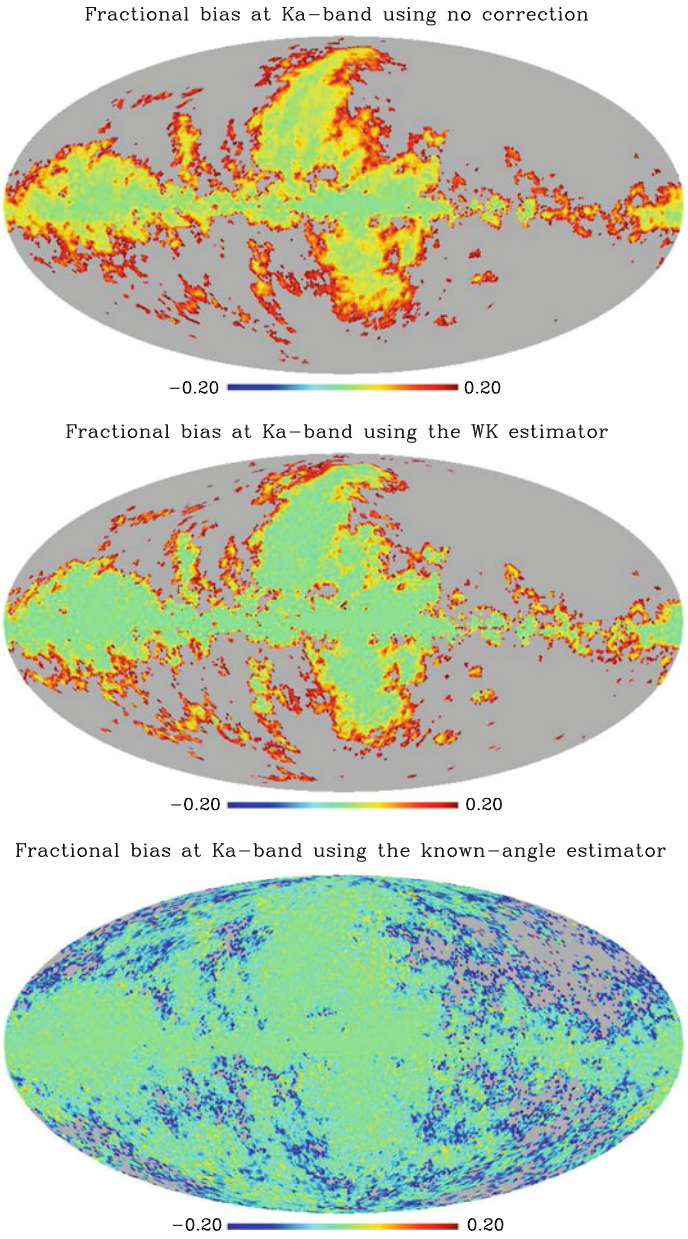

Fig. 2.18 Maps showing the fractional bias at Ka-band. On *top* is the polarisation bias for the naive estimator $P = \sqrt{Q^2 + U^2}$. At the *centre* is the residual bias that remains after correcting with the $\hat{p}_{WK}$ estimator. At the *bottom* is the residual bias that remains after correcting with the $\hat{p}_{\chi}$ estimator. All the pixels with an absolute value larger than 20 % (0.2 in the map units) are shown in *grey*

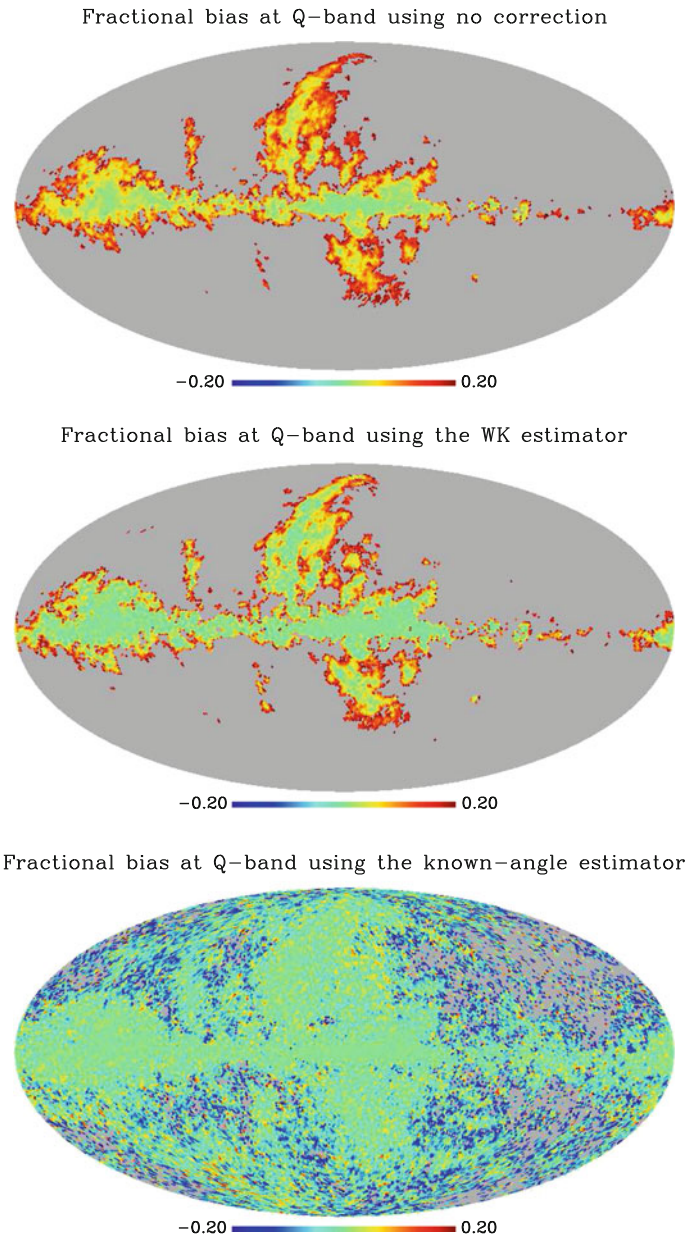

Fig. 2.19 Same as Fig. 2.18 but for *WMAP* Q-band

Table 2.3 Percentage of the area of the full-sky map that have an absolute value of the residual fractional bias smaller than 0.2

Estimator	K-band (%)	Ka-band (%)	Q-band (%)
p_0	84.9	35.0	18.4
p_{WK}	94.7	68.0	42.9
p_χ	–	84.8	84.3

These areas corresponds to the coloured pixels in Figs. 2.17, 2.18 and 2.19

By looking at the unmasked (not grey) areas of Figs. 2.18 and 2.19, we can see that the $\hat{p}_\chi$ estimator performs better than the $\hat{p}_{WK}$ one, as there are much more pixels within the $[-0.2, 0.2]$ range in fractional bias. In Table 2.3 we lists the percentage of the area of the sky with a residual fractional bias smaller than ± 0.2.

2.5.5 *Bias-Corrected Polarisation Maps*

We prepared bias-corrected polarisation amplitude maps of *WMAP* K, Ka and Q-bands maps, smoothed to a common resolution of 3°. For K-band, we used the modified Wardle and Kronberg formula shown in Eq. 2.22 (Fig. 2.20).

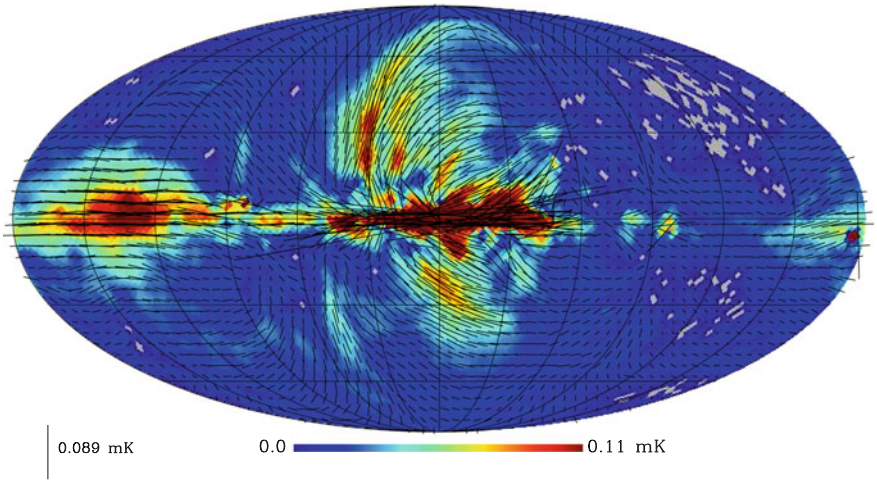

Fig. 2.20 Bias-corrected polarisation amplitude maps of *WMAP* K, Ka and Q-bands. The masked area (*grey pixels*) corresponds to the regions where the uncertainty in the polarisation amplitude is larger than the polarisation amplitude so the estimator value is imaginary (see Eq. 2.22). The maps have an angular resolution 3° and the units are thermodynamic Kelvin. The length of the vectors are proportional to the polarisation amplitude (see scale) and their direction is parallel to the magnetic field

Given the nature of the de-biasing method we use for Ka and Q bands—the knowledge of the true polarisation angle—we have masked out the pixels from the K-band map where the uncertainties in (Q, U) would convert to an uncertainty in the polarisation angle, χ, larger than 6°. This value was chosen to be sure that the residual bias will be smaller than 5 %, as shown with the simulations in the previous Section.

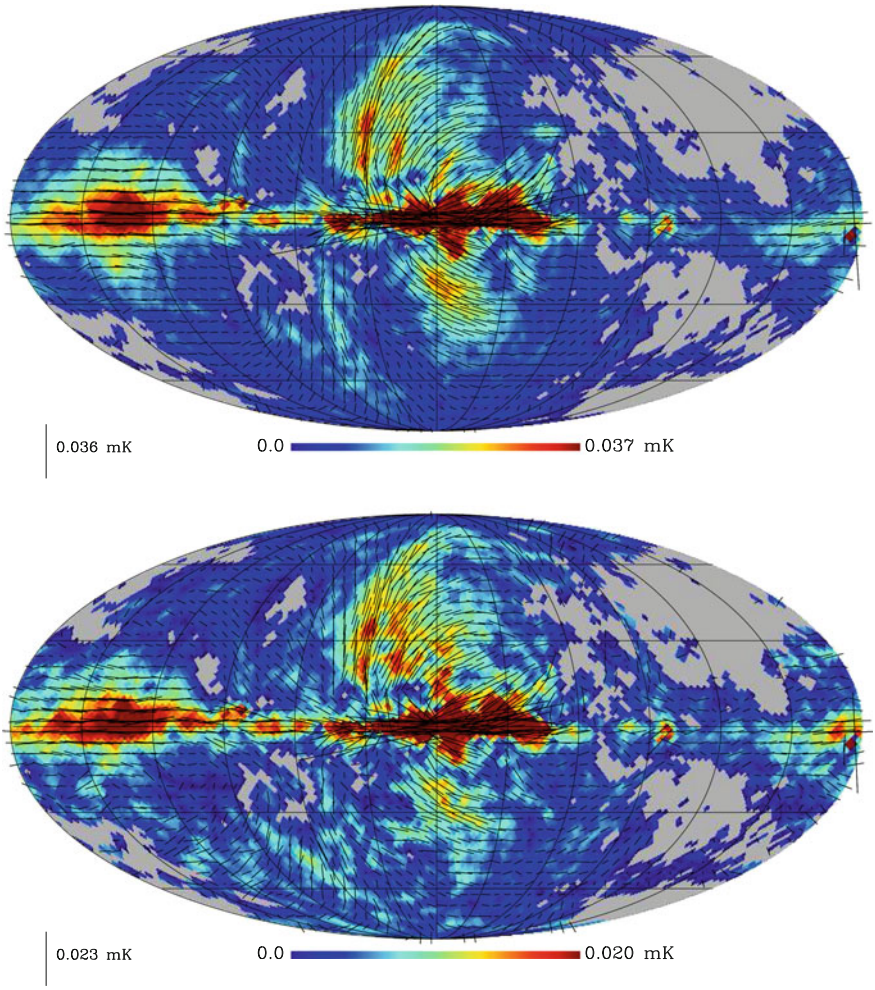

Fig. 2.21 Bias-corrected polarisation amplitude maps of *WMAP* K, Ka and Q-bands. The masked area (grey pixels) corresponds to the region where the uncertainty in the polarisation angle at K-band is larger than 9°. The maps have an angular resolution 3° and the units are thermodynamic Kelvin. The length of the vectors are proportional to the polarisation amplitude (see scale) and their direction is parallel to the magnetic field

This corresponds to a masked area of 17.7 %. In Fig. 2.21 we show the maps, with the masked areas shown as grey. Also plotted on each map are the polarisation vectors, aligned parallel to the magnetic field direction (we have rotated the vectors by 90°).

2.6 Polarisation Upper Limits from AME Regions

Here we summarize the work presented in Dickinson et al. (2011). We used a different de-biasing method to derive upper limits for the fractional polarisation of AME in two molecular clouds. The method used here is a generalisation of the one developed by Vaillancourt (2006) which using Bayesian analysis to estimate the true polarisation amplitude. We modified the method to allow for assymetric uncertainties.

The ρ Ophiuchi and Perseus molecular clouds are two of the most conspicuous AME regions in the Galaxy. Planck Collaboration et al. (2011) describes an analysis in total intensity and showed that these regions are dominated by AME in the 20–60 GHz frequency range. The temperature spectra observed by *Planck* can be fitted using spinning dust models. Here, we used *WMAP* seven-year data to constrain the AME polarisation fraction in these clouds.

We smoothed the maps to a common resolution of 1° using the procedure described in Sect. 2.3. Aperture photometry was used to extract flux densities from the *WMAP* maps. We chose a circular aperture of 2° to calculate the fluxes. A background level was subtracted by estimating the median value inside an annulus with inner radius equal to 80′ and an outer radius of 120′. Figures 2.22 and 2.23 show the I, Q, U, P and polarisation angle maps at the *WMAP* bands for the Perseus and ρ Ophiuchi regions respectively. The integration regions used for the photometry are also shown in the Figures.

The ρ Ophiuchi and Perseus regions are bright sources in intensity maps. Because of this, it is important to test for any potential leakage from Stokes I to Q, U. The *WMAP* team corrects the maps for this leakage. A map of spurious signal, the S map, is calculated using the fact that the intensity leakage does not depend on the orientation of the spacecraft, it only depends on the intensity and spectral shape of the intensity source (Barnes et al. 2003). We measured the polarised signal of the Orion Nebula (M42), a bright un-polarised source to check the leakage level. It has a value $\lesssim$0.1 % at K-band, and it is even smaller at the higher frequencies. We therefore do not include an additional contribution to the uncertainty in polarisation due to leakage.

The noise in the smoothed Q, U maps was derived using Monte Carlo simulations, which include the correlated terms between Q and U. Then, the polarisation flux densities were corrected for the polarisation bias. We list in Table 2.4 the flux densities for the ρ Ophiuchi and Perseus clouds in all the *WMAP* bands for Stokes I, Q, U and polarisation amplitude. The de-biased polarisation amplitude is very low in both clouds (less than 3σ at all frequencies). We can only place upper limits for the polarisation fraction giving the noise of the data. The limits for the fractional

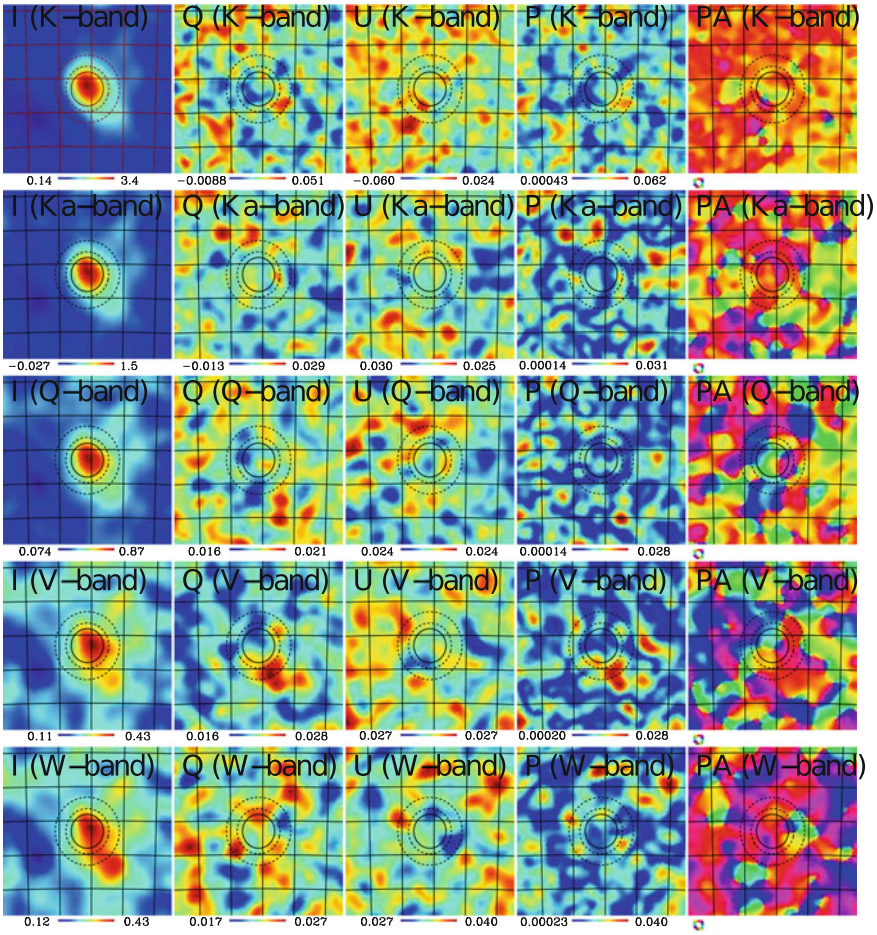

Fig. 2.22 *WMAP* 7-year maps of the Perseus region at the five *WMAP* bands. Each map covers $10° \times 10°$ centred at $(l, b) = (353.°05, +16.°90)$ and is smoothed to 1° resolution. From *left* to *right* are Stokes I (total intensity), Q, U, polarized intensity (P) and polarization angle (PA). Units are thermodynamic (CMB) mK. The graticule has a spacing of 2°. The primary extraction aperture is shown as a *solid line* and the background annulus as a *dashed line*

polarisation of AME in ρ Ophiuchi are 1.7, 1.6 and 2.6 % while in the Perseus clouds are 1.4, 1.9 and 4.7 % at K, Ka and Q bands respectively.

These limits rule out some emission mechanism for the AME. Magnetic dipole radiation can exhibit high ($\sim$>10 %) polarization at 20–40 GHz when there is a single magnetic domain (Draine and Lazarian 1999). The polarisation fraction limits we found are not compatible with this model.

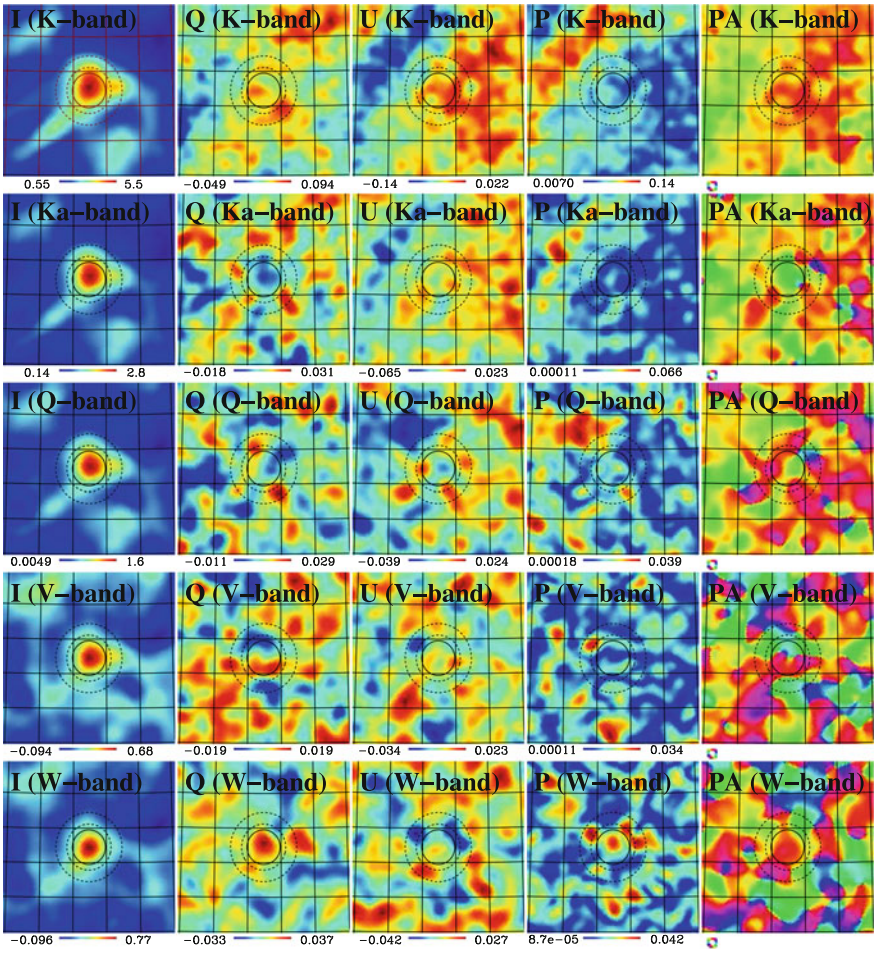

Fig. 2.23 *WMAP* 7-year maps of the ρ Ophiuchi region at the five *WMAP* bands. Each map covers $10^\circ \times 10^\circ$ centred at $(l, b) = (353\overset{\circ}{.}05, +16^\circ.90)$ and is smoothed to 1° resolution. From *left* to *right* are Stokes I (total intensity), Q, U, polarized intensity (P) and polarization angle (PA). Units are thermodynamic (CMB) mK. The graticule has a spacing of 2°. The primary extraction aperture is shown as a *solid line* and the background annulus as a *dashed line*

If these limits of polarisation fraction are typical for AME at high Galactic latitudes, the only important polarisation emission at frequencies under 100 GHz would be synchrotron, therefore simplifying the CMB polarised foreground characterisation.

Table 2.4 Aperture photometry of the *WMAP* 7-year maps in the ρ Ophiuchi (*top*) and Perseus (*bottom*) molecular cloud regions, using a 2° diameter aperture

Frequency (GHz)	I (Jy)	I_{sd} (Jy)	Q (Jy)	U (Jy)	P (Jy)	P_0 (Jy)	Π (%)	Π_{sd}(%)
22.7 (K-band)	26.3 ± 5.5	24.8 ± 6.6	0.091 ± 0.096	0.23 ± 0.14	0.25 ± 0.13	0.21 ± 0.11(<0.43)	<1.6	<1.7
33.0 (Ka-band)	30.7 ± 5.3	27.2 ± 6.3	-0.27 ± 0.12	0.02 ± 0.15	0.27 ± 0.12	0.24 ± 0.12(<0.44)	<1.4	<1.6
40.7 (Q-band)	27.7 ± 4.6	21.9 ± 5.8	-0.07 ± 0.18	-0.23 ± 0.24	0.24 ± 0.23	0.00 ± 0.30(<0.57)	<2.1	<2.6
60.6 (V-band)	26.3 ± 4.5	9.8 ± 6.5	0.35 ± 0.41	0.41 ± 0.40	0.54 ± 0.41	0.00 ± 0.61(<1.1)	<4.2	<11
93.4 (W-band)	63.6 ± 8.9	6 ± 15	2.8 ± 1.0	0.0 ± 1.7	2.8 ± 1.0	2.6 ± 1.0	4.1 ± 1.8	...
22.7 (K-band)	21.0 ± 3.1	16.7 ± 3.5	-0.118 ± 0.071	0.068 ± 0.069	0.136 ± 0.070	0.11 ± 0.06(< 0.24)	<1.1	<1.4
33.0 (Ka-band)	20.4 ± 3.0	15.7 ± 3.3	0.02 ± 0.13	-0.06 ± 0.15	0.07 ± 0.15	0.0 ± 0.15(<0.30)	<1.5	<1.9
40.7 (Q-band)	16.9 ± 2.9	11.6 ± 3.3	0.07 ± 0.19	-0.25 ± 0.21	0.26 ± 0.21	0.0 ± 0.30(<0.54)	<3.2	<4.7
60.6 (V-band)	14.9 ± 4.0	5.4 ± 4.4	0.098 ± 0.077	-0.64 ± 0.59	0.65 ± 0.39	0.4 ± 0.27(<1.2)	<8.1	<22
93.4 (W-band)	32.4 ± 9.8	3 ± 10	-0.5 ± 1.3	-0.3 ± 2.3	0.6 ± 1.4	0.0 ± 1.5(< 2.9)	<9.0	...

The columns contain flux densities for intensity I, the spinning dust contribution to the intensity (I_{sd}), Q, U, the observed polarized intensity (P), the maximum likelihood value for the noise-bias corrected polarized intensity (P_0), the total fraction (Π), and the polarization fraction for spinning dust (Π_{sd}). Upper limits are at the 95 % c.l

References

Barnes, C., et al. (2003). First-Year Wilkinson Microwave Anisotropy Probe (WMAP) observations: Galactic signal contamination from sidelobe pickup. *ApJS*, *148*, 51–62.

Bennett, C. L., et al. (2013). Nine-year Wilkinson Microwave Anisotropy Probe (WMAP) observations: Final maps and results. *ApJS*, *208*(20), 20.

Delabrouille, J., et al. (2013). The pre-launch Planck SkyModel: a model of sky emission at submillimetre to centimetre wavelengths. *A & A*, *553*(A96), A96.

Dickinson, C., Peel, M., & Vidal, M. (2011). New constraints on the polarization of anomalous microwave emission in nearby molecular clouds. *MNRAS*, *418*, L35–L39.

Draine, B. T., & Lazarian, A. (1999). Magnetic dipole microwave emission from dust grains. *ApJ*, *512*, 740–754.

Fixsen, D. J. (2009). The temperature of the cosmic microwave background. *ApJ*, *707*, 916–920.

Górski, K. M., et al. (2005). HEALPix: A framework for high-resolution discretization and fast analysis of data distributed on the sphere. *ApJ*, *622*, 759–771.

Haslam, C. G. T., et al. (1982). A 408 MHz all-sky continuum survey. II—The atlas of contour maps. *A & AS*, *47* 1.

Hinshaw, G., et al. (2003). First-Year Wilkinson Microwave Anisotropy Probe (WMAP) observations: Data processing methods and systematic error limits. *ApJS*, *148*, 63–95.

Jarosik, N., et al. (2003). First-Year Wilkinson Microwave Anisotropy Probe (WMAP) observations: On-orbit radiometer characterization. *ApJS*, *148*, 29–37.

Mather, J. C., et al. (1999). Calibrator design for the COBE Far-Infrared Absolute Spectrophotometer (FIRAS). *ApJ*, *512*, 511–520.

Miville-Deschênes, M.-A., et al. (2008). Separation of anomalous and synchrotron emissions using WMAP polarization data. *A & A*, *490*, 1093–1102.

Naghizadeh-Khouei, J., & Clarke, D. (1993). On the statistical behaviour of the position angle of linear polarization. *A & A, 274*, 968.

Planck Collaboration et al. (2011). Planck early results. XX. New light on anomalous microwave emission from spinning dust grains. *A & A, 536*, A20, A20.

Quinn, J. L. (2012). Bayesian analysis of polarization measurements. *A & A, 538*, A65, A65.

Serkowski, K. (1958). Statistical analysis of the polarization and reddening of the double cluster in perseus. *Acta Astron, 8*, 135.

Simmons, J. F. L., & Stewart, B. G. (1985). Point and interval estimation of the true unbiased degree of linear polarization in the presence of low signal-to-noise ratios. *A & A*, *142*, 100–106.

Vaillancourt, J. E. (2006). Placing confidence limits on polarization measurements. *PASP*, *118*, 1340–1343.

Vinokur, M. (1965). Optimisation dans la recherche d'une sinusode de période connue en présence de bruit. Application à la radioastronomie. *Annales d'Astrophysique, 28*, 412.

Wardle, J. F. C., & Kronberg, P. P. (1974). The linear polarization of quasi-stellar radio sources at 3.71 and 11.1 centimeters. *ApJ*, *194*, 249–255.

Wehus, I. K., Fuskeland, U., & Eriksen, H. K. (2013). The effect of systematics on polarized spectral indices. *ApJ*, *763*(138), 138.

http://www.springer.com/978-3-319-26262-8

Diffuse Radio Foregrounds
All-Sky Polarisation, and Anomalous Microwave Emission
Vidal Navarro, M.
2016, XLIV, 196 p. 124 illus., 28 illus. in color.,
Hardcover
ISBN: 978-3-319-26262-8